

Higher-Dimensional Information Lattice: Quantum State Characterization through Inclusion-Exclusion Local Information

Ian Matthias Flór,¹ Claudia Artiaco,^{1,2} Thomas Klein Kvorning,¹ and Jens H. Bardarson¹

¹*Department of Physics, KTH Royal Institute of Technology, Stockholm, 106 91 Sweden*

²*Institut für Theoretische Physik, Universität zu Köln,
Zülpicher Straße 77, D-50937 Cologne, Germany*

We generalize the information lattice, originally defined for one-dimensional open-boundary chains, to characterize quantum many body states in higher-dimensional geometries. In one dimension, the information lattice provides a position- and scale-resolved decomposition of von Neumann information. Its generalization is nontrivial because overlapping subsystems can form loops, allowing multiple regions to encode the same information. This prevents information from being assigned uniquely to any one of them. We address this by introducing a higher-dimensional information lattice in which local information is defined through an inclusion-exclusion principle. The inclusion-exclusion local information is assigned to the lattice vertices, each labeled by subsystem position and scale. We implement this construction explicitly in two dimensions and apply it to a range of many-body ground states with distinct entanglement structures. Within this position- and scale-resolved framework, we extract information-based localization lengths, direction-dependent critical exponents, characteristic edge mode information, long-range information patterns due to topological order, and signatures of non-Abelian fusion channels. Our work establishes a general information-theoretic framework for isolating the universal scale-resolved features of quantum many-body states in higher-dimensional geometries.

I. INTRODUCTION

A useful way to think about a quantum state is through its correlation structure: how information is distributed across its different parts. Quantum information quantities are independent of any particular choice of observables, giving access to universal properties of quantum states and making their correlation structures explicit, regardless of the underlying physical details. As a result, quantum information theory has become a central framework for understanding quantum systems, with methods now widely applied in fields ranging from condensed-matter physics [1–3] and quantum computing [4, 5] to holographic approaches to quantum gravity [6–8].

In condensed-matter physics, quantum information and entanglement provide a natural approach to characterizing states and phases [2, 3]. For instance, the von Neumann entropy of a subsystem is a standard diagnostic of the universality class of a state. In one-dimensional (1D) systems, it is constant with subsystem size (that is, area law) in ground states of local gapped Hamiltonians, while it exhibits a universal logarithmic scaling at criticality [9–12]. In midspectrum states of ergodic Hamiltonians it instead scales with the subsystem length (that is, volume law) [13–15]. The central role of quantum information quantities in quantum many-body physics is also reflected in the success of numerical methods such as tensor networks, which exploit the 1D area law of von Neumann entropy to efficiently represent ground states of local gapped Hamiltonians [16–18]. However, the von Neumann entropy is a single number that quantifies the total correlation between a subsystem and its complement. It does not by itself specify how correlations are distributed among locations, scales, or degrees of freedom. This has motivated a range of approaches aiming to construct lo-

cal or spatially resolved descriptions of quantum correlations. Approaches in this direction include various multipartite entanglement measures [19–21], quantum Fisher information [22–26], entanglement contour [27–29] and entanglement link representation [30–32], as well as local descriptions of von Neumann entropy dynamics such as the entanglement quasiparticle picture [33–35], the membrane picture [36, 37], and the entanglement tsunami [38].

Among these efforts, the recently introduced *information lattice* provides a fully local decomposition of information for one-dimensional quantum states [39, 40]. It decomposes information, understood as the average number of binary questions one can answer by knowing the system state, into *local information*, which is the information in a subsystem that is not contained in any subsystem of smaller scale or different location. Thus, local information is labeled by the subsystem position within the physical chain and by the subsystem length (or scale). The evolution of local information on the information lattice under local unitary dynamics follows continuity-like equations with well-defined information currents. This unique hydrodynamic property for information has been used to analyze quenches [41–43] and to construct efficient time-evolution algorithms [39, 44, 45]. The underlying idea of those algorithms is to distinguish relevant from irrelevant quantum information based on its scale, and in turn use this to simulate the dynamics of large-scale many-body systems by discarding irrelevant long-range correlations. In the same spirit, several other methods have been recently developed, such as the density-matrix truncation method [46–51], dissipation-assisted operator evolution [52–56], approaches that trade entanglement for mixtures [57, 58], cluster truncated Wigner approaches [59], and other discussions of the entanglement barrier [60, 61]. Furthermore, the local decompo-

sition provided by the information lattice makes it possible to isolate short-scale contributions from long-scale ones. This defines universality classes of quantum states (e.g., localized, critical, ergodic, topological) through the distribution of the total information per scale and allows one to quantify the intrinsic state length scales [40]. Moreover, this local information perspective extends beyond entanglement and provides a witness for long-range magic [62].

Higher dimensional quantum states can host much richer information structures than their one-dimensional counterparts. For example, in higher dimensions subsystems admit various shapes and topologies, and the interval-based ordering that constrains many 1D entanglement constructions is no longer available [31, 63–67]. The increase in dimensionality is accompanied by phenomena absent in 1D systems, such as extended Fermi surfaces, topologically ordered phases [68], or the possibility of braiding anyons [69–71]. Distinguishing state universality classes from the scaling of the subsystem von Neumann entropy is often less direct compared to in 1D. In low entangled states, the von Neumann entropy is dominated by the area-law contributions, while universal features are often contained in subleading geometry-dependent terms at quantum critical points [72–75], in a multiplicative logarithm for states with a Fermi surface [76–80], or as a constant offset in topologically ordered phases [81, 82]. The increased geometric complexity is also reflected in computational approaches: projected entangled pair states are a conceptually direct generalization of matrix product states, but their contraction and optimization are substantially more demanding and lack a simple canonical form [83, 84]. Many of these challenges can be traced to the increased connectivity of the underlying higher-dimensional geometry, and as such are fundamentally unavoidable.

Generalizing the information lattice to higher dimensions similarly faces intrinsic challenges tied to geometry. In 1D, the notion of scale is fixed by the subsystem length, which provides a natural starting point for defining information-based characteristic length scales. In higher dimensions, subsystems of comparable size come in many inequivalent shapes, and there is no canonical ordering or hierarchy of subsystems from which to begin such a scale assignment. The underlying question is whether information can be assigned uniquely to a given location and scale in the presence of overlapping subsystems. In higher dimensions, and already in 1D periodic chains, subsystems can overlap in a loop-like manner, a feature absent for open-boundary 1D chains. As a result, the same information can be accessed from multiple distinct overlapping subsystems. We refer to this phenomenon as *overlap redundancy*. Overlap redundancies are nonlocal information structures that are not specific to quantum mechanics, as they already appear in multivariate classical information theory [85–87]. In this work, we introduce a higher-dimensional information lattice that treats overlap redundancies as part of the struc-

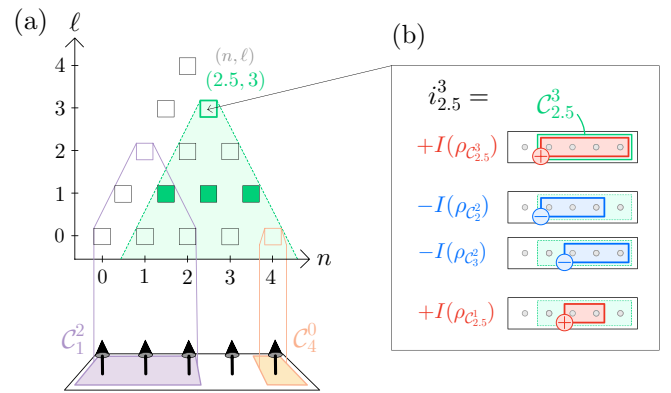


FIG. 1. On a 1D chain of five physical sites [indicated by black arrows at the bottom of (a)], we consider the subsystems C_n^ℓ consisting of $\ell + 1$ consecutive sites centered at position n on the chain. Each subsystem is labeled by the indices (n, ℓ) , which in (a) are represented as square vertices and arranged hierarchically in a triangular structure. Examples are shown for C_1^2 in lilac and C_4^0 in yellow. The local information i_n^ℓ is calculated for each vertex (n, ℓ) by an addition-subtraction of the subsystem von Neumann information [see Eq. (4)] as illustrated in (b) for $i_{2,5}^3$. The shaded green area in (b) represents the subsystem $C_{2,5}^3$. The shaded green area in (a) includes all the vertices associated with subsystems contained within $C_{2,5}^3$. The total information in $C_{2,5}^3$ is the sum of all the local information i_n^ℓ associated with the vertices within the shaded green area in (a) [see Eq. (3)]. The filled green vertices label all the subsystems of scale 1 which are contained in the larger subsystem $C_{2,5}^3$. The total information at scale $\ell = 1$ in $C_{2,5}^3$ is the sum of all local information i_n^ℓ on the filled green vertices [see Eq. (5)].

ture, providing a hierarchical position- and scale-resolved description of how information is organized in quantum many-body states.

Our higher-dimensional information lattice defines the inclusion-exclusion local information, which characterizes quantum states in any spatial dimension. After introducing the construction and discussing the role of overlap redundancies (Sec. II), we explicitly implement the framework in 2D using rectangular subsystems (Sec. III). We then illustrate its use on representative quantum many-body states with distinct entanglement characteristics, including a localized state and a critical state with a Fermi surface (Sec. IV A), a system with a chiral 1D edge mode (Sec. IV B), and a topologically ordered state both with and without non-Abelian defects (Sec. IV C). Our framework is universal and applies to arbitrary quantum states, including mixed states. In Sec. V, we summarize our findings and discuss possible future directions.

II. GENERALIZING THE INFORMATION LATTICE TO HIGHER DIMENSIONS

The von Neumann information (or total information) of a state ρ is

$$I(\rho) = \log_2(\dim \rho) - S(\rho) \quad (1)$$

where $\dim \rho$ is the Hilbert space dimension of the state and $S(\rho) = -\text{Tr}[\rho \log_2 \rho]$ is the von Neumann entropy. $I(\rho)$ is the average number of bits that can be inferred from ρ about the distribution of measurement outcomes [88]. Analogously, the von Neumann information of the reduced density matrix $\rho_C = \text{Tr}_{\bar{C}}\rho$, defined by

$$I(\rho_C) = \log_2(\dim \rho_C) - S(\rho_C), \quad (2)$$

is the total information in the subsystem C , that is, the number of bits that can be inferred from ρ_C about measurements supported on C . The total information $I(\rho_C)$ in a subsystem C also accounts for the information already present in its subsystems $C' \subset C$.

A. The 1D information lattice

Before generalizing the information lattice to higher-dimensional systems, we briefly review its construction in the 1D case. While the total information of a subsystem includes that of all its parts, in a 1D chain the *local information* quantifies the information that is exclusive to a given subsystem, namely that it cannot be found in any subsystem at a lower scale or different location. The *information lattice* organizes the local information of each subsystem according to its spatial location and its length scale [39–41, 44, 45].

To achieve a decomposition of the information into local contributions from different subsystems, one considers the collection of all subsystems $\{\mathcal{C}_n^\ell\}$ of $\ell+1$ neighboring sites centered at position n on the one-dimensional chain. Each subsystem is uniquely identified by a label (n, ℓ) . The set of labels can be placed on a triangular structure illustrated in Fig. 1(a), where each vertex (square marker) is associated with the position n along the physical chain (horizontal axis) and the scale ℓ (vertical axis). This defines a hierarchical arrangement, where the labels associated with larger subsystems are placed at higher levels. The information lattice decomposes the von Neumann information of a subsystem \mathcal{C}_n^ℓ into a sum of individual contributions $i_n^{\ell'}$ for each subsystem $\mathcal{C}_{n'}^{\ell'} \subset \mathcal{C}_n^\ell$ through

$$I(\rho_{\mathcal{C}_n^\ell}) = \sum_{\{(n', \ell') | \mathcal{C}_{n'}^{\ell'} \subseteq \mathcal{C}_n^\ell\}} i_{n'}^{\ell'}. \quad (3)$$

For example, $I(\rho_{\mathcal{C}_{2,5}^3})$ is the sum of the values $i_{n'}^{\ell'}$ on all subsystems covered by the shaded green area in Fig. 1(a).

Imposing that the above condition be satisfied for all subsystems results in i_n^{ℓ} taking the form

$$i_n^{\ell} = I_n^\ell - I_{n-1/2}^{\ell-1} - I_{n+1/2}^{\ell-1} + I_n^{\ell-2}, \quad (4)$$

where I_n^ℓ is a shorthand for $I(\rho_{\mathcal{C}_n^\ell})$. This subtraction of von Neumann information values is represented schematically in Fig. 1(b). The expression of i_n^{ℓ} in Eq. (4) corresponds to the quantum conditional mutual information [89]; i_n^{ℓ} singles out the portion of information that is exclusive to scale ℓ and position n . The quantum conditional mutual information is greater than or equal to zero by the strong subadditivity of von Neumann entropy [90]. If $i_n^{\ell} = 0$, the outcome distribution of an optimal measurement on \mathcal{C}_n^ℓ is already fixed by the reduced density matrices of its two smaller subsystems $\rho_{\mathcal{C}_{n\pm1/2}^{\ell-1}}$ [91]: no new bits of information are gained by performing measurements on the larger subsystem \mathcal{C}_n^ℓ . If $i_n^{\ell} > 0$, the state $\rho_{\mathcal{C}_n^\ell}$ contributes exactly i_n^{ℓ} additional bits beyond those contained in its smaller subsystems. Thus, i_n^{ℓ} is a local quantity in position and scale that singles out the portion of information unique to \mathcal{C}_n^ℓ [39–41, 44, 45].

By summing the local information i_n^{ℓ} over the positional indices n , we obtain information per scale quantities [40]. The information at scale ℓ' inside a subsystem \mathcal{C}_n^ℓ is

$$I(\ell')|_{\mathcal{C}_n^\ell} = \sum_{\{n' | \mathcal{C}_{n'}^{\ell'} \subseteq \mathcal{C}_n^\ell\}} i_{n'}^{\ell'}. \quad (5)$$

For example, the information in $\mathcal{C}_{2,5}^3$ at scale $\ell' = 1$ is the sum of the local information over the filled green vertices in Fig. 1(a). This captures the exclusive information at scale ℓ' inside \mathcal{C}_n^ℓ since it tells us how many extra bits can be inferred about outcomes at scale ℓ' from all density matrices at scale ℓ' , compared with what can be learned from only those at scale $\ell' - 1$.

B. Inclusion-Exclusion Information

The starting point of our generalization of the 1D information lattice to higher dimensions is the decomposition of the information (3) on a selection of subsystems. The perspective of the information decomposition allows us to recast the problem of defining local information for each individual subsystem into that of choosing a set of subsystems ordered in position and scale appropriately. The most direct generalization is to consider the set of all connected subsystems which differ from each other by a single site, as in the 1D case. However, the 1D information lattice benefits from the fact that an intersection of any two subsystems is labeled by its own vertex on the lattice. This is a necessary condition to achieve a correct scale-assignment of information [92], which we therefore also impose on our set of subsystems in higher dimensions. In higher dimensions, the intersection of subsystems generically yields disconnected subsystems, unless

the subsystems are convex (contain every shortest lattice path between any two of their sites). This leaves us with two possibilities. The first is to consider a lattice whose vertices also label disconnected subsystems. However, this causes the number of vertices to grow exponentially with system size and adds a complication in the purpose of a scale-resolved description of information. The second option is to impose that the subsystems are convex. We define the higher-dimensional information lattice by considering a set of convex subsystems. We denote those subsystems as \mathcal{C}_n^ℓ with

- a multiscale label ℓ , which encodes the spatial extent of a subsystem along independent axes;
- a positional label n , which locates the subsystem within the system.

When clear from context, we will refer to ℓ as the scale. The subsystems in the set $\{\mathcal{C}_n^\ell\}$ are partially ordered by all $n_i \in \mathbf{n}$ and $\ell_i \in \ell$, where increasing ℓ corresponds to enlarging subsystems in one or more dimensions. The most natural choice of subsystems depends on the geometry of the physical system. For instance, on a 2D square lattice it is natural to consider rectangular subsystems specified by position (n_x, n_y) and scale (ℓ_x, ℓ_y) (see next section), whereas in a radial geometry one may instead use coordinates (n_r, n_θ) and scales (ℓ_r, ℓ_θ) . We impose the decomposition property (3) on this set of subsystems. The decomposition (3) represents a system of equations where $i_{n'}^{\ell'}$ are the unknowns. Its solution is obtained by so-called Möbius inversion [93, 94] and is given by the expression

$$i_n^\ell = I(\rho_{\mathcal{C}_n^\ell}) - \sum_{i \in \mathcal{I}_n^\ell} I(\rho_{\mathcal{A}_i}) + \sum_{i < j \in \mathcal{I}_n^\ell} I(\rho_{\mathcal{A}_i \cap \mathcal{A}_j}) - \sum_{i < j < k \in \mathcal{I}_n^\ell} I(\rho_{\mathcal{A}_i \cap \mathcal{A}_j \cap \mathcal{A}_k}) + \dots, \quad (6)$$

where \mathcal{I}_n^ℓ is the set of indices of subsystems $\mathcal{A}_i \subset \mathcal{C}_n^\ell$ obtained by removing one layer of sites (i.e., decreasing one of the components of ℓ by one) along any coordinate direction. The second term subtracts the information from pairwise intersections of the subsystems \mathcal{A}_i . Subsequent terms alternately add and subtract the information from the higher-order intersections between three or more subsystems \mathcal{A}_i , which correspond to progressively smaller subsystems in \mathcal{C}_n^ℓ . We refer to (6) as the *inclusion-exclusion local information*, and when clear from context as local information for short. We require the set of subsystems to be closed under intersections; that is, for any two subsystems $\mathcal{C}_{n_1}^{\ell_1}$ and $\mathcal{C}_{n_2}^{\ell_2}$ in the set, their intersection $\mathcal{C}_{n_1}^{\ell_1} \cap \mathcal{C}_{n_2}^{\ell_2}$ must also belong to the set.

Note that if the position and scale of the set of subsystems is only varied along one axis, Eq. (6) reduces to an expression similar to the 1D local information (4). We detail such quasi-1D constructions in Sec. III.

C. Overlap redundancies in higher dimensions

In the 1D information lattice, the subsystems $\{\mathcal{C}_n^\ell\}$ are not only closed under intersections but they also form a set chain at each scale ℓ : the set $\{\mathcal{C}_n^\ell\}_{\text{all } n}$ satisfies $(\bigcup_{m < n} \mathcal{C}_m^\ell) \cap \mathcal{C}_n^\ell = \mathcal{C}_{n-1}^\ell \cap \mathcal{C}_n^\ell$ [95]. In that case, i_n^ℓ in Eq. (4) can be expressed as the quantum conditional mutual information

$$I(A : C|B) = I(\rho_{ABC}) - I(\rho_{AB}) - I(\rho_{BC}) + I(\rho_B) \quad (7)$$

between A and C conditioned on B . Indeed, comparing with Eq. (4), ABC denotes \mathcal{C}_n^ℓ , and the subsystems $A = \mathcal{C}_{n-\ell/2}^0$, $B = \mathcal{C}_{n-\ell/2}^{\ell-2}$ and $C = \mathcal{C}_{n+\ell/2}^0$ are disjoint. In geometries other than the open 1D chain, the set of subsystems $\{\mathcal{C}_n^\ell\}$ in Eq. (6) closed under intersections typically does not form a set chain. For example, when the subsystems at one scale form a loop $\{AB, BC, CA\}$ the inclusion-exclusion information takes the form

$$I(A : B : C) = I(\rho_{ABC}) - I(\rho_{AB}) - I(\rho_{BC}) - I(\rho_{AC}) + I(\rho_A) + I(\rho_B) + I(\rho_C). \quad (8)$$

Eq. (8) is a possible multipartite generalization of the conditional mutual information, known as the *interaction information*, among the disjoint subsystems A, B, C [85–87, 96–100]. Unlike Eq. (7), $I(A : B : C)$ may be negative. A positive value signals that the state on ABC contains new correlations present in ρ_{ABC} that are absent from all reduced density matrices. Conversely, a negative value signals a *redundancy* between the density matrices on $\{AB, BC, CA\}$, meaning the distribution of measurement outcomes on a subsystem can be partially inferred from the density matrices on the other two. In classical terms, this corresponds to the situation where conditioning on one variable reduces the dependence between the others, expressed as $I(A : C|\emptyset) > I(A : C|B)$ with \emptyset the empty set [101]. Analogous to the loop $\{AB, BC, CA\}$, the subsystems in the set $\{\mathcal{C}_n^\ell\}_{\text{all } n}$ at a given multiscale ℓ in (6) overlap in space but do not form a set chain. A negative value of the inclusion-exclusion information i_n^ℓ signals there is redundancy among the density matrices, we refer to this as an *overlap redundancy* at that scale. Note that while a negative value necessarily implies an overlap redundancy, the reverse may not be true; overlap redundancies could be present even if i_n^ℓ is positive; in such a case, there are more additional correlations than redundancy between lower scale density matrices.

We illustrate an overlap redundancy through a simple three qubit example. We first consider the state $\rho_{abc} = \frac{1}{2}(|\uparrow\uparrow\uparrow\rangle\langle\uparrow\uparrow\uparrow| + |\downarrow\downarrow\downarrow\rangle\langle\downarrow\downarrow\downarrow|)$ on three qubits labeled a, b, c in an open 1D chain. The qubits and their respective positions are shown in Fig. 2(a) (bottom). The total information of the state is $I(\rho_{abc}) = 2$ bits. In Fig. 2(a), those two bits are decomposed on the 1D information lattice by evaluating (4). We see that at $\ell = 0$ the single site subsystems contribute no information $i_a^0 = i_b^0 = i_c^0 = 0$ (their density matrices are maximally mixed). The $\ell = 1$ subsystems each contribute $i_{ab}^1 = i_{bc}^1 = 1$ bit,

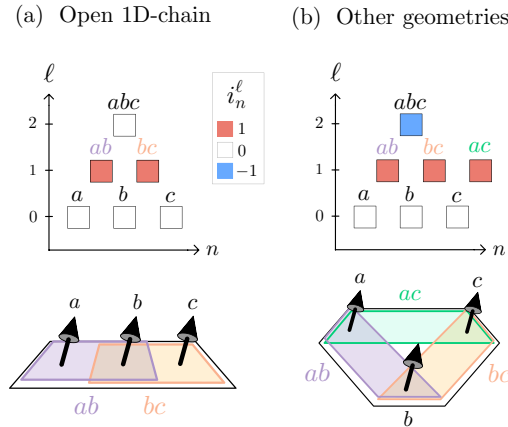


FIG. 2. (a) 1D chain of three qubits denoted a, b, c (bottom) in the state $\rho_{abc} = \frac{1}{2}(|\uparrow\uparrow\uparrow\rangle\langle\uparrow\uparrow\uparrow| + |\downarrow\downarrow\downarrow\rangle\langle\downarrow\downarrow\downarrow|)$. The 1D information lattice (top) is represented for this state, where for clarity the names of the subsystems are shown next to the vertices that label them (as a , ab , and so on). It shows that local information is exclusively located at scale $\ell = 1$ in subsystems ab and bc that have 1 bit each, and the total information in the state is 2 bits given by the sum of those two contributions. (b) Consider the same state ρ_{abc} for a system in a triangular arrangement (bottom). There are three two-site subsystems, the new one being ac (green). (Top) On the information lattice based on the inclusion-exclusion information (6) at scale $\ell = 1$ each subsystem contributes 1 bit of information. However, 1 out of these 3 bits is redundant; the 2 bits of information are contained in any pair of $\rho_{ab}, \rho_{bc}, \rho_{ac}$. Using Eq. (6), the overcounting of this redundant information at scale $\ell = 1$ is compensated by a negative value at scale $\ell = 2$, the scale at which all overlapping subsystems are contained and the dependence in their correlations is resolved.

so summing all information at scale $\ell = 1$ according to (5) already gives the total information of 2 bits in the state. Correspondingly, there are $i_{abc}^2 = 0$ new bits at the largest scale. The 1D information lattice unambiguously shows that all the information about the state ρ_{abc} is contained in ab and bc , as we cannot better predict the distribution of measurement outcomes on abc from ρ_{abc} than can already be inferred from the density matrices ρ_{ab} and ρ_{bc} .

We now consider the same state on three qubits a, b, c , but in a triangular arrangement as shown in Fig. 2(b) (bottom) (for instance, on a periodic 1D-chain or a higher-dimensional lattice) and examine the information that contributes to certain scales. At $\ell = 1$ in Fig. 2(b) (top), each of the three two-site subsystems provides 1 bit of information. This time, summing their individual contributions following (5) gives 3 bits, which exceeds the total information of the state. This shows that in the decomposition (6) the same information may be accounted for redundantly by overlapping subsystems. This occurs when the density matrices $\rho_{ab}, \rho_{bc}, \rho_{ac}$ are not independent. In this example, any one of the three density matrices can be reconstructed from the other two, e.g., ρ_{ac}

adds no new information about measurement outcomes on abc compared to ρ_{ab} and ρ_{bc} . In other words, the 2 bits of information in the full state ρ_{abc} are shared by all three two-site density matrices.

The redundancy arises from attributing too much information to a particular scale, where a set of density matrices are mutually dependent. The decomposition property (3) ensures that the surplus information assigned to a given scale is subtracted at the larger scale that fully encompasses the redundant correlation. In the three site triangular example in Fig. 2, the inclusion-exclusion information at scale $\ell = 2$ is

$$i_{abc}^2 = I(a : b : c) = -1 \text{ bit.} \quad (9)$$

This negative value is shown in Fig. 2(b) (top) at scale $\ell = 2$: the subsystem abc , being the smallest that contains all overlapping subsystems, reflects the redundancy and compensates with exactly -1 bit. The presence of overlap redundancies means that the same information about the state can be obtained from spatially distinct overlapping subsystems. While this nonlocal character of an overlap redundancy is a feature of non-chain geometries, the appearance of a negative value is still a property of the state: a negative value indicates that some of the subsystems at a lower scale share the same information nonlocally. Rather than an obstruction, overlap redundancies provide a visible signature of how information is structured in the state. Note that in this three-subsystem case, Eq. (8) coincides with the Kitaev formula for topological entanglement entropy [81], if one assumes that A, B and C are subsystems larger than the correlation length. This is not a coincidence: the topological entanglement entropy quantifies precisely a global information redundancy in topologically ordered ground states, as we come back to in Sec. IV C.

III. THE 2D INFORMATION LATTICE USING RECTANGULAR SUBSYSTEMS

In the remainder, we evaluate the inclusion-exclusion information (6) on rectangular subsystems on two-dimensional lattices to illustrate the key features of our method. However, the construction itself can be applied in arbitrary dimensions and one is free to pick whichever set of subsystems closed under intersections.

A. Rectangular inclusion-exclusion information

We consider a system of $N_x \times N_y$ physical sites arranged on a square lattice as shown for a 4×4 system in Fig. 3(a) (right). Instead of connected intervals in 1D, we now consider rectangular subsystems \mathcal{C}_n^ℓ in 2D which are labeled by the coordinate of their bottom-left corner $\mathbf{n} = (n_x, n_y)$ and their scale $\ell = (\ell_x, \ell_y)$, where a scale ℓ_x corresponds to a subsystems that extends over $\ell_x + 1$ physical sites along the x direction and $\ell_y + 1$

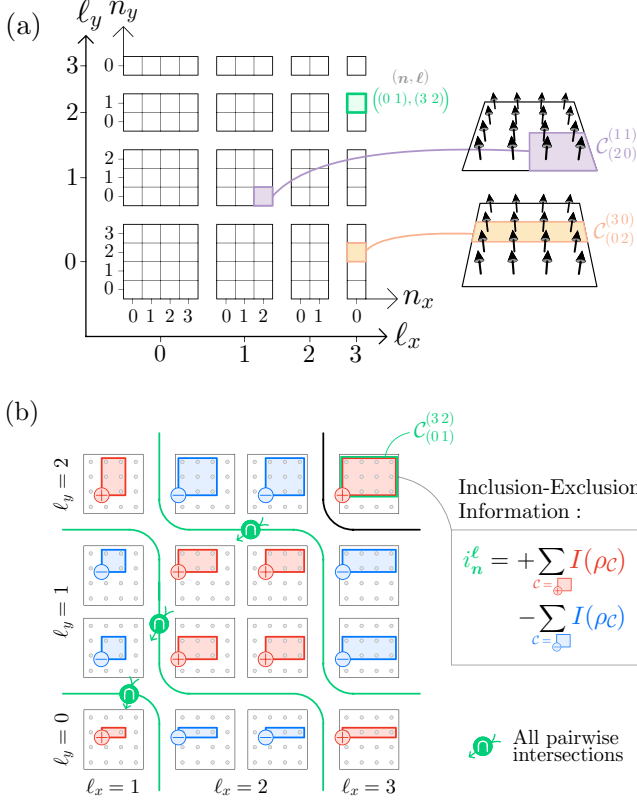


FIG. 3. (a) On a system of 4×4 physical sites (black arrows), each rectangular subsystem is labeled by its scale $\ell = (\ell_x \ell_y)$ and the coordinate of its bottom-left corner $\mathbf{n} = (n_x n_y)$, denoted as $\mathcal{C}_{(n_x n_y)}^{(\ell_x \ell_y)}$ (for example $\mathcal{C}_{(0,0)}^{(1,1)}$ in lilac and $\mathcal{C}_{(0,0)}^{(3,0)}$ in yellow). Each subsystem label is represented by a square marker on a lattice, where they are ordered across scales and positions as shown on the left. (b) For every subsystem, we compute its inclusion-exclusion information i_n^ℓ in Eq. (10). The structure of the inclusion-exclusion equation is illustrated for the subsystem $\mathcal{C}_{(0,1)}^{(3,2)}$. We first take the total information in $\mathcal{C}_{(0,1)}^{(3,2)}$ and then subtract (blue) the information of the subsystems at scales $(3,1)$ and $(2,2)$ [first and second lines in (10)]. The information from all pairwise subtractions (indicated by crossing the green curve) must be re-added (red) [third line in (10)]. Higher-order intersections are re-subtracted and re-added until only one set is left. The green line separates levels of the inclusion-exclusion order of intersections: the subsystems to the left are intersections of those to the right (marked by the direction of the green arrow).

physical sites along the y direction. We represent each pair (\mathbf{n}, ℓ) by a vertex (square marker) in Fig. 3(a) labeling the subsystems $\mathcal{C}_{\mathbf{n}}^\ell$. This mapping between vertices and subsystems is illustrated for the subsystems $\mathcal{C}_{(2,0)}^{(1,1)}$ and $\mathcal{C}_{(0,2)}^{(3,0)}$ in Fig. 3(a). The inclusion-exclusion information (6) can be evaluated for the rectangular subsystems, which

explicitly gives

$$\begin{aligned}
i_n^\ell &= I_n^\ell \\
&- \left(I_n^{\ell-(1,0)} + I_{n+(1,0)}^{\ell-(1,0)} + I_n^{\ell-(0,1)} + I_{n+(0,1)}^{\ell-(0,1)} \right) \\
&+ \left(I_n^{\ell-(1,1)} + I_{n+(1,0)}^{\ell-(1,1)} + I_{n+(0,1)}^{\ell-(1,1)} + I_n^{\ell-(1,1)} + I_{n+(1,0)}^{\ell-(2,0)} + I_{n+(0,1)}^{\ell-(0,2)} \right) \\
&- \left(I_{n+(1,0)}^{\ell-(2,1)} + I_{n+(1,1)}^{\ell-(2,1)} + I_{n+(0,1)}^{\ell-(1,2)} + I_{n+(1,1)}^{\ell-(1,2)} \right) \\
&+ I_{n+(1,1)}^{\ell-(2,2)}
\end{aligned} \tag{10}$$

for each pair (\mathbf{n}, ℓ) , where I_n^ℓ is the von Neumann information of the reduced density matrix on the subsystem $\mathcal{C}_{\mathbf{n}}^\ell$. The evaluation of (10) is represented visually in Fig. 3(b) for the vertex $(\mathbf{n}, \ell) = (0,1), (3,2)$: the first line in (10) is the total information in $\mathcal{C}_{(0,1)}^{(3,2)}$. The second line of (10) subtracts the information of the next smaller subsystems [i.e., those at scales $(\ell_x - 1, \ell_y)$ and $(\ell_x, \ell_y - 1)$]. Then, the information of all possible pairwise intersections [separated by a green line and an intersection symbol in Fig. 3(b)] is re-added in the third line. The last two lines in (10) re-subtract and re-add the information of higher order intersections. The inclusion-exclusion equation bears some similarity with a finite-difference expression. In fact, the above can simplify to a finite-difference expression in some cases [102]. In Eq. (10), it is implicitly assumed that a subsystem with indices ℓ_x or ℓ_y smaller than zero is empty, with zero information.

We illustrate the 2D information lattice with a simple state on a lattice of 6×6 sites, in which all sites are in the spin-up configuration, except for two entangled pairs

$$|\Psi_{\text{singlets}}\rangle = \left(\bigotimes_{\substack{(n_x n_y) \notin \{(0,0), \\ (2,2), (0,4), (4,3)\}}} |\uparrow\rangle_{(x,y)} \right) \otimes |\Psi_-\rangle_{(0,0),(2,2)} \otimes |\Psi_-\rangle_{(0,4),(4,3)} \tag{11}$$

where $|\Psi_-\rangle_{(n_x n_y), (n'_x n'_y)} = \frac{1}{\sqrt{2}} (|\uparrow\rangle_{(n_x n_y)} |\downarrow\rangle_{(n'_x n'_y)} - |\downarrow\rangle_{(n_x n_y)} |\uparrow\rangle_{(n'_x n'_y)})$ denotes a singlet between the sites positioned at (n_x, n_y) and (n'_x, n'_y) [these positions are connected by blue lines in Fig. 4(a)]. A single-site subsystem carries 1 bit of information when the site is unentangled (its density matrix is pure) but 0 bits when it belongs to a singlet (the density matrix is maximally mixed). This is what the distribution of information shows in the lowest scale $\ell = (0,0)$ of the information lattice in Fig. 4(a). Each entangled pair contributes 2 bits of information at the smallest scale that encompasses it entirely: in this case $|\Psi_-\rangle_{(0,0),(2,2)}$ is fully enclosed in the subsystem $\mathcal{C}_{(0,0)}^{(2,2)}$ and $|\Psi_-\rangle_{(0,4),(4,3)}$ in $\mathcal{C}_{(0,3)}^{(4,1)}$. Operationally, 1 bit is, e.g., associated with the measurement of $\hat{X}\hat{X}$ on a given singlet, which yields the outcome -1 with certainty, while the other bit is associated with the measurement of $\hat{Y}\hat{Y}$, which yields $+1$, for the Pauli operators \hat{X} and \hat{Y} .

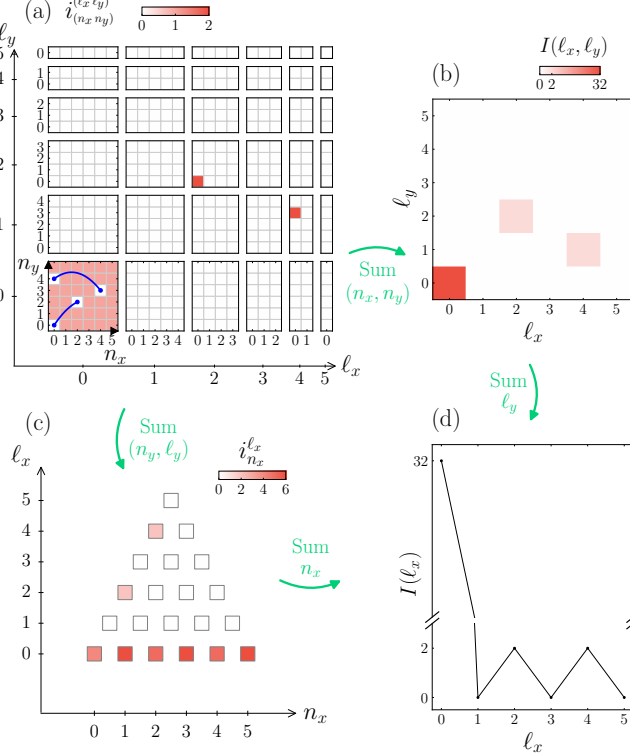


FIG. 4. (a) We decompose the information of the state (11), consisting of all sites in a spin-up configuration except for four sites forming two singlets (illustrated by the blue lines), by evaluating the inclusion-exclusion information in Eq. (10). For each vertex $((n_x n_y), (\ell_x \ell_y))$ (square marker), the inclusion-exclusion information $i_{(n_x n_y)}^{(\ell_x \ell_y)}$ is represented by a color. The information of the singlets is captured at the smallest scales that fully enclose them (at $((00), (22))$ and $((03), (41))$ respectively). (b) Summing out $(n_x n_y)$ leaves the total scale resolved information of the state $I(\ell_x, \ell_y)$: 32 bits are at (00) while 2 bits are found at (22) and 2 others at (41) . (c) Summing out an axis $(n_y \ell_y)$ leaves a quasi-1D information lattice over scales $(n_x \ell_x)$, where the information of the state is only resolved along the x direction. (d) Summing (b) over ℓ_y or (c) over n_x gives the quasi-1D information per scale along ℓ_x .

B. Reduced information quantities

In analogy with the information per scale Eq. (5) for 1D, we define reduced information quantities in 2D by partial summations over indices. We define the information at scale ℓ' inside of a subsystem \mathcal{C}_n^ℓ as

$$I(\ell')|_{\mathcal{C}_n^\ell} = \sum_{\{\mathbf{n}' | \mathcal{C}_{n'}^{\ell'} \subseteq \mathcal{C}_n^\ell\}} i_{\mathbf{n}'}^{\ell'}, \quad (12)$$

which we abbreviate as $I(\ell_x, \ell_y)$ or $I(\ell)$ when \mathcal{C}_n^ℓ is the whole system. $I(\ell_x, \ell_y)$ is illustrated in Fig. 4(b) for the singlets state in Eq. (11): it shows that most information is in the single site scales while two bits appear at two intermediate scales. We can also consider partial summations over an entire axis, which leaves us with a quasi-1D

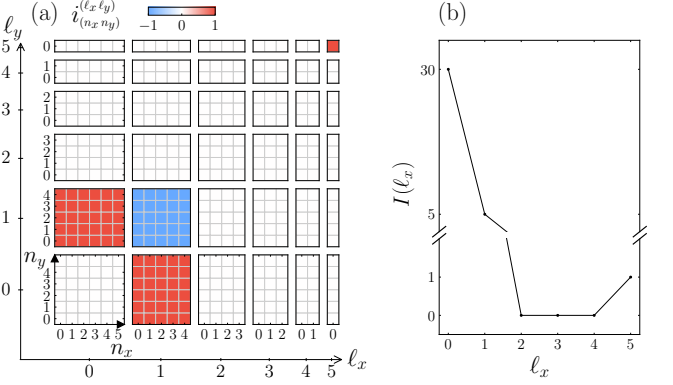


FIG. 5. (a) 2D information lattice of the cat state defined in Eq. (16), where the reading of the lattice is identical to Fig. 4(a). There are now negative values at scale $\ell = (1, 1)$, which compensate for the over-counting of information at scales $\ell = (1, 0)$ and $(0, 1)$. This signals that the overlapping subsystems at those lower scales have dependent density matrices, what we call an overlap redundancy. (b) The quasi-1D information per scale along the x direction defined in (14) resolves the information along the x direction, and therefore it is insensitive to loop redundancies. Both (a) and (b) show a bit at the largest scale: in cat states a bit of information cannot be inferred by any local measurement and requires access to the entire system.

information lattice along the remaining axis. For example, summing over the y axis inside a subsystem \mathcal{C}_n^ℓ

$$i_{n'_x}^{\ell'}|_{\mathcal{C}_n^\ell} = \sum_{\{(n'_y, \ell'_y) | \mathcal{C}_{n'}^{\ell'} \subseteq \mathcal{C}_n^\ell\}} i_{n'_y}^{\ell'}, \quad (13)$$

is the quasi-1D local information inside \mathcal{C}_n^ℓ , which we abbreviate as $i_{n'_x}^{\ell'}$ when \mathcal{C}_n^ℓ is the whole system. Analogously to the 1D local information (4), the quasi-1D local information (13) can be conveniently placed on a triangular structure with vertices labeled by (n'_x, ℓ'_x) ; this is illustrated in Fig. 4(c) for $i_{n'_x}^{\ell'}$. The quasi-1D information lattice tells us that 2 bits become accessible at position and scale $(n_x, \ell_x) = (0, 2)$ and also at $(n_x, \ell_x) = (0, 4)$, but leaves out the resolution along the y direction. Finally, we define the quasi-1D information at scale ℓ'_x inside \mathcal{C}_n^ℓ by summing over the position n'_x in Eq. (13), or equivalently by summing over the scale ℓ'_y in Eq. (12),

$$I(\ell'_x)|_{\mathcal{C}_n^\ell} = \sum_{n'_x} i_{n'_x}^{\ell'}|_{\mathcal{C}_n^\ell}, \quad (14)$$

which we abbreviate as $I(\ell_x)$ when \mathcal{C}_n^ℓ is the whole system. This tells us the scale in the x direction at which information became accessible.

C. General quasi-1D constructions

The quasi-1D information quantities defined in Eqs. (13) and (14) are nonnegative. This can be seen

by substituting Eq. (10) in (13), which simplifies into

$$i_{n'_x}^{\ell'_x} |_{\mathcal{C}_n^\ell} = I_n^\ell - I_n^{\ell-(10)} - I_{n+(10)}^{\ell-(10)} + I_{n+(10)}^{\ell-(20)}. \quad (15)$$

This has an identical form to the 1D local information (4). Here, the y direction has been coarse grained: the physical sites along y are grouped together to form a new elementary site with enlarged Hilbert space; the quasi-1D local information then captures correlations only along x . To illustrate this we use the cat state

$$|\Psi_{\text{cat}}\rangle = \frac{1}{\sqrt{2}} (|\uparrow\uparrow\cdots\uparrow\rangle + e^{i\phi}|\downarrow\downarrow\cdots\downarrow\rangle) \quad (16)$$

placed on 6×6 qubits with relative angle $\phi = 0$. The reduced density matrices of $|\Psi_{\text{cat}}\rangle$ have the form $\frac{1}{2}(|\uparrow\uparrow\cdots\uparrow\rangle\langle\uparrow\uparrow\cdots\uparrow| + |\downarrow\downarrow\cdots\downarrow\rangle\langle\downarrow\downarrow\cdots\downarrow|)$ on each subsystem. The negative information values at scale $\ell = (1 1)$ in Fig. 5(a) show that there is an information redundancy. Indeed, the density matrices at scales $\ell = (1 0)$ and $\ell = (0 1)$ are not independent (they are precisely those discussed in Sec. II C). This contrasts with the quasi-1D information per scale in the x direction (14) shown in Fig. 5(b). As in 1D, (15) quantifies how much more information can be inferred about the distribution of measurement outcomes on \mathcal{C}_n^ℓ from $\rho_{\mathcal{C}_n^\ell}$ than what can be inferred from the two smaller density matrices $\{\rho_{\mathcal{C}_n^{\ell-(10)}}, \rho_{\mathcal{C}_{n+(10)}^{\ell-(10)}}\}$ on the subsystems that are reduced by a single unit along the x direction. The bit of information at the largest scale is present in both cases, as the phase ϕ can only be learned globally and is invisible to any local measurement.

We note that quasi-1D generalizations can also be constructed by directly selecting subsystems ordered along a one-dimensional position n and scale ℓ (that is, by considering set chains in higher-dimensions), and evaluating the local information [Eq. (4)] as in 1D. Fig. 6 illustrates two such constructions: one obtained by coarse graining the y direction, and another by coarse graining concentric square rings around the system center.

IV. CHARACTERIZING QUANTUM STATES THROUGH THE 2D INFORMATION LATTICE

Quantum states of one-dimensional chains are universally characterized by their distribution of local information [40]. Building on this, we show how the inclusion-exclusion information (6) specialized to rectangular subsystems (10) can be used to characterize quantum states in two-dimensional systems.

A. Localized and critical ground states of the 2D Anderson model

We consider the ground state $|\Psi_{\text{AM}}\rangle$ of the disordered Anderson model (AM) [103, 104] on a two-dimensional

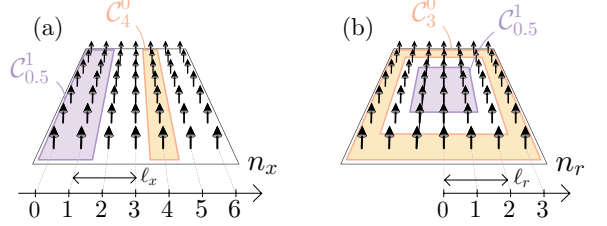


FIG. 6. In the information lattice, a higher-dimensional system can be treated as effectively one-dimensional by evaluating the local information [Eq. (4)] along a chosen 1D direction (specified by position n and scale ℓ) while coarse graining the other directions into a single site with an enlarged Hilbert space: this yields a *quasi-1D information lattice*. (a) illustrates this construction for subsystems $\mathcal{C}_{n_x}^{\ell_x}$ at different horizontal positions n_x and scales ℓ_x (e.g., $\mathcal{C}_{0.5}^1$ in lilac and \mathcal{C}_4^0 in orange), with the y direction coarse grained. This produces the quasi-1D local information $i_{n_x}^{\ell_x}$ from Eq. (15). (b) shows an analogous construction where Eq. (4) resolves correlations along the radial direction, treating concentric square rings $\mathcal{C}_{n_r}^{\ell_r}$ (radius n_r , thickness ℓ_r) as the sites of a 1D chain. For instance, \mathcal{C}_0^3 (orange) is a ring centered at square radius $n_r = 3$ with thickness $\ell_r = 1$, whereas $\mathcal{C}_{0.5}^1$ (lilac) is a ring at $n_r = 0.5$ whose thickness $\ell_r = 1$ makes it coincide with a filled square at the origin.

square lattice of size $N_x \times N_y$ defined by the Hamiltonian

$$\hat{H}_{\text{AM}} = - \sum_i (t_x \hat{c}_i^\dagger \hat{c}_{i+\hat{x}} + t_y \hat{c}_i^\dagger \hat{c}_{i+\hat{y}} + \text{H.c.}) + \sum_i \epsilon_i \hat{c}_i^\dagger \hat{c}_i, \quad (17)$$

where \hat{c}_i^\dagger (\hat{c}_i) creates (annihilates) an electron at site i , and ϵ_i are independent random onsite potentials uniformly distributed in $[-W/2, W/2]$ with disorder strength W . The unit vectors \hat{x} and \hat{y} connect each site i to its nearest neighbors in the horizontal and vertical directions with hopping amplitudes t_x and t_y that may differ to allow for anisotropy. We work at half filling. Since \hat{H}_{AM} is noninteracting, the von Neumann information of the subsystem density matrices of $|\Psi_{\text{AM}}\rangle$ can be efficiently calculated from the single-particle eigenstates [105]. At zero disorder ($W = 0$), the eigenstates are extended and the ground state is a gapless critical state. In one dimension and in two dimensions for symmetry classes such as the orthogonal and unitary classes, any nonzero uncorrelated disorder $W > 0$ produces exponentially localized states [106, 107]. By contrast, in three dimensions a localization-delocalization transition occurs at a finite disorder strength even for uncorrelated disorder, whereas in two dimensions this happens only in special symmetry classes such as the symplectic class [107]. Here we consider the ground state in both the localized phase ($W \neq 0$) and the clean case ($W = 0$) of the 2D Anderson model in the orthogonal class.

In 1D systems, localized states are characterized by an exponential decay of the information per scale (5), from which a *correlation decay length* λ can be defined as an intrinsic measure of localization [40]. In two dimensions,

we analogously define the correlation decay lengths λ_μ for $\mu \in \{x, y\}$ by a least-squares fit of the quasi-1D information per scale $I(\ell_\mu)$ as

$$\ln I(\ell_\mu) = -\ell_\mu/\lambda_\mu + \text{const.} \quad (18)$$

To illustrate this we consider the ground state $|\Psi_{\text{AM}}\rangle$ for a single disorder realization of the Hamiltonian (17) with anisotropic hopping $t_x = 1.5$ and $t_y = 1$, and $W = 10$ on a lattice of $N_x \times N_y = 40 \times 40$ sites. The information per multiscale is illustrated in Fig. 7(a), showing an elliptically shaped profile at short scales, characteristic of localized states. The corresponding quasi-1D information per scale is shown in Fig. 7(c), together with least-squares exponential fits to extract λ_μ along both directions. The correlation decay lengths offer a system-agnostic characterization of localization that can be extracted from the density matrix and they also apply in interacting states.

We now turn to the gapless critical ground state in the clean case ($W = 0$). Unlike in 1D, where criticality is fully captured by the scale invariance of local information [40], higher-dimensional critical states exhibit substantially richer behavior [3]. To examine the critical behavior, we first adopt a quasi-1D reduction: we treat the y -axis as an internal degree of freedom and analyze scale invariance along \hat{x} (and vice versa). In this reduced description, the critical ground state is scale invariant in the sense of Ref. [40], which implies

$$I(\ell_\mu) \propto \ell_\mu^{-2}. \quad (19)$$

This power law is represented in Fig. 7(d), where it is only represented for $I(\ell_x)$ for visibility.

To go beyond the quasi-1D reduction, we examine the information per multiscale in Fig. 7(b). We find that the information extends preferentially along a specific scale direction. We define the *information propagation direction* $\langle \hat{v} \rangle$ through a least-squares fit as the direction of maximum variance [108]

$$\langle \hat{v} \rangle = \arg \max_{\|\alpha\|=1} \alpha^\top \Sigma \alpha \quad (20)$$

where $\Sigma = \sum_{\ell} I(\ell) \ell \ell^\top / \sum_{\ell} I(\ell)$ is the 2×2 information per multiscale weighted covariance matrix. $\langle \hat{v} \rangle$ is the normalized eigenvector of Σ with the largest eigenvalue: the unit vector along which a scale increase yields the largest information gain. The inclusion-exclusion information $i_{\hat{n}}^{\ell}$ decays with a power of -2 for values of ℓ along $\langle \hat{v} \rangle$ (not shown). In general, the information per multiscale may extend along several directions. The fit Eq. (20) identifies the dominant among these directions by construction, providing a single effective information propagation direction. In our case, this dominant direction is clearly visible in Fig. 7(b) as the bright, anisotropic feature extending along a direction close to the diagonal. The information per multiscale displays a weaker contribution to the information along ℓ_x for subsystems with $\ell_y = 0$. This contribution originates from the horizontal 1D chains embedded in the 2D system, including those

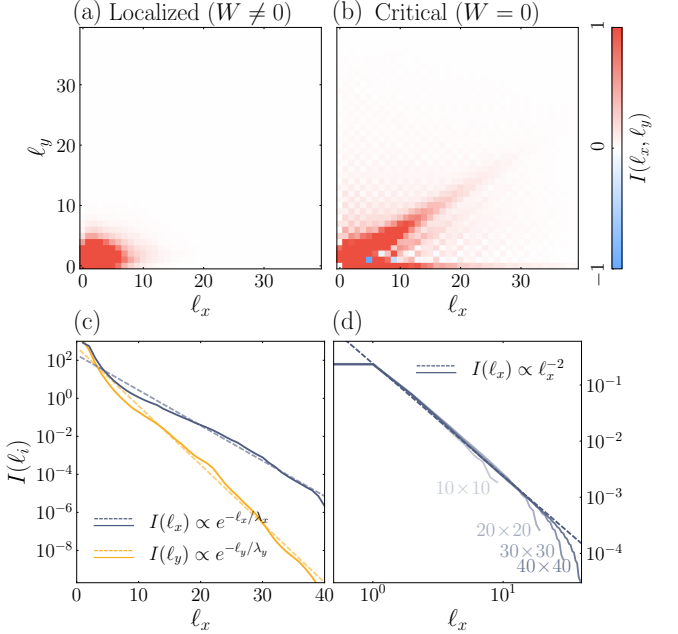


FIG. 7. Inclusion-exclusion information (10) of the ground state of the Anderson model on a 40×40 lattice with hopping amplitudes $t_x = 1.5$ and $t_y = 1$ [see Eq. (17)]. (Left) For a single disorder realization at $W = 10$, panel (a) shows the information per multiscale, concentrated at short scales. The anisotropy results in a larger spread of information along the ℓ_x direction. Panel (c) displays the quasi-1D information per scale $I(\ell_\mu)$ along x and y (solid lines, gray and orange respectively). Exponential fits (18) (dashed lines) yield the correlation decay lengths λ_x and λ_y that characterize the 2D localized phase. (Right) For $W = 0$, the ground state is critical. (d) The quasi-1D information per scale (solid lines, for multiple system sizes) follows the 1D scale-invariant form $I(\ell_x) \propto \ell_x^{-2}$ (a similar behavior holds along ℓ_y , not shown), with the fitted power law indicated by a dashed line. In panel (b), the information per multiscale is oriented along a dominant direction, which we refer to as the information propagation direction.

in the bulk. In the fully anisotropic limit of $t_y = 0$, the 2D system reduces to decoupled critical horizontal 1D chains. In this case, the inclusion-exclusion information at scale $\ell_y = 0$ (horizontal chains) decays with a power law $\propto \ell_x^{-2}$, while at scale $\ell_x = 0$ (vertical chains) there is no information gain along the ℓ_y direction. This scaling behaviour is observed in the weakly anisotropic case considered here as well (scaling $\propto \ell_x^{-2}$ not shown). We leave a full characterization of why this scaling persists beyond this limit to future work.

The information propagation direction is the direction along which enlarging the subsystem yields the greatest increase in information. We note a correspondence with the Fermi velocity orientation, suggesting that this direction captures the critical modes responsible for long-range entanglement in gapless states. Motivated by the Widom formula [76–78], which relates entanglement to the momentum orientations on the Fermi surface rela-

tive to the subsystem boundary, we express an average Fermi velocity direction specialized to rectangular subsystems [109] as

$$\langle \hat{v}_F \rangle \propto \int_{\mathbf{k} \in \text{FS}} \left(\frac{|\hat{v}_F^x(\mathbf{k})|}{|\hat{v}_F^y(\mathbf{k})|} \right) ds, \quad (21)$$

where the omitted proportionality factor is such that $\langle \hat{v}_F \rangle$ is normalized. Here $|\cdot|$ denotes the absolute value, $\hat{v}_F^\mu(\mathbf{k})$ is the $\mu \in \{x, y\}$ component of the normalized Fermi velocity and ds is the length element along the Fermi surface $\text{FS} = \{\mathbf{k} \mid t_x \cos k_x + t_y \cos k_y = 0\}$ for the tight-binding model (17) with $W = 0$ and at half-filling. The information gain is largest when the subsystem multiscale is increased along $\langle \hat{v}_F \rangle$. To illustrate this, we analyze the scale dependence of the inclusion-exclusion information $i_{(0,0)}^{(\ell_x, \ell_y)}$ of a single subsystem, located at the bottom left corner of the system. We consider three values of t_x with fixed $t_y = 1$ on a system of $N_x \times N_y = 25 \times 40$ sites, which allows us to change the Fermi surface. In the isotropic case $t_x = 1$, the Fermi surface is diamond shaped and $\langle \hat{v}_F \rangle = (1, 1)/\sqrt{2}$ [see inset of Fig. 8(a)]. The corresponding information gain is maximal along this direction [Fig. 8(a)]. For $t_x = 1.1$, the deformation of the Fermi surface tilts $\langle \hat{v}_F \rangle$, and the information propagation direction tilts accordingly [Fig. 8(b)]. For stronger anisotropy, $t_x = 2.5$, the information propagation direction is mostly along the x -axis, again consistent with the direction of $\langle \hat{v}_F \rangle$ [Fig. 8(c)]. These observations illustrate that the inclusion-exclusion information provides a natural way to identify dominant propagation directions in critical states of higher-dimensional systems. A systematic analysis of these critical directions based on a renormalization approach to scale invariance in the 2D information lattice is left for future work.

B. Gapped bulk with a critical edge in the chiral $p_x + ip_y$ superconductor

In the previous section, we considered a 2D free-fermion system whose Fermi surface gives rise to gapless excitations throughout the bulk. In contrast, we now consider a gapped 2D system whose bulk excitations are fully gapped while its boundary supports a single chiral edge mode. An example of such a system is the ground state $|\Psi_{\text{TSC}}\rangle$ of the spinless chiral $p_x + ip_y$ topological superconductor [110–113], given on a square lattice by the Bogoliubov-de-Gennes Hamiltonian [114]

$$\begin{aligned} \hat{H}_{\text{TSC}} = & -\mu \sum_i \hat{c}_i^\dagger \hat{c}_i - t \sum_{i, \hat{n} \in \{\hat{x}, \hat{y}\}} (\hat{c}_i^\dagger \hat{c}_{i+\hat{n}} + \text{H.c.}) \\ & + \frac{\Delta}{2} \sum_i (\hat{c}_i \hat{c}_{i+\hat{x}} + \text{H.c.}) + i \frac{\Delta}{2} \sum_i (\hat{c}_i \hat{c}_{i+\hat{y}} - \text{H.c.}) \end{aligned} \quad (22)$$

Here, μ is the chemical potential, t is the hopping amplitude, and Δ the pairing strength. For $|\mu| > 4t$, the

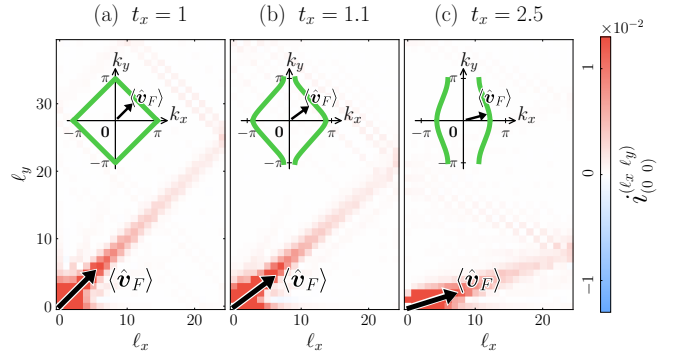


FIG. 8. Inclusion-exclusion information $i_{(0,0)}^{(\ell_x, \ell_y)}$ (colormap) of a subsystem positioned at the bottom-left corner of the system, as its scale (ℓ_x, ℓ_y) increases, in the ground state of the anisotropic Anderson model (17) at half-filling and at criticality $W = 0$ on a lattice of $N_x \times N_y = 25 \times 40$ sites. It is shown for (a) $t_x = 1$, (b) $t_x = 1.1$, and (c) $t_x = 2.5$ with $t_y = 1$. Insets show the Fermi surface in the Brillouin zone for each case (assuming periodic boundary conditions) together with the propagation direction $\langle \hat{v}_F \rangle$ obtained by evaluating the average Fermi vector direction Eq. (21) from the analytical expression of the Fermi surface. The same vectors $\langle \hat{v}_F \rangle$ are represented in the main panels, where they show agreement with the information propagation direction (20). This demonstrates that the dominant propagation in the information per multiscale points in the average direction of the velocity of the chiral modes on the Fermi surface.

ground state is topologically trivial and short-range correlated with Chern number $C = 0$. For $|\mu| < 4t$, the ground state is in a chiral topological phase supporting a single chiral Majorana edge mode whose direction of propagation (chirality) reverses as μ changes sign [115–117] (here Majorana edge mode refers to the collective edge excitation which, unlike Majorana zero modes, need not occur in pairs [118]).

The quasi-1D information per scale [Eq. (14)] for the ground states in the trivial ($\mu = 6t, C = 0$) and topological ($\mu = 2t, C = 1$) phases is shown in Fig. 9(c) and (d), respectively. We set $\Delta = t = 1$. In the trivial ground state, $I(\ell_x)$ decays exponentially, signaling localized behavior, while in the topological ground state $I(\ell_x)$ decays algebraically, signaling critical behavior. The corresponding information per multiscale is shown in Fig. 9(a) and (b). Both states exhibit sharply peaked information at small multiscales. In the topological state, we note the presence of negative values at scales $\ell_x = 2$ or $\ell_y = 2$. They indicate that the same information can be accessed in overlapping subsystems at lower scales but different locations, similar to what is encountered at the short scales of the cat state in Fig. 5. Furthermore, the information contribution of horizontal ($\ell_y = 0$) and vertical ($\ell_x = 0$) 1D chain subsystems extends further across length scales. Unlike in Sec. IV A, where chain subsystem contributions at these scales originated from both the bulk and the edge subsystems, here they come only from the edge ones.

To demonstrate the spatial origin of these contribu-

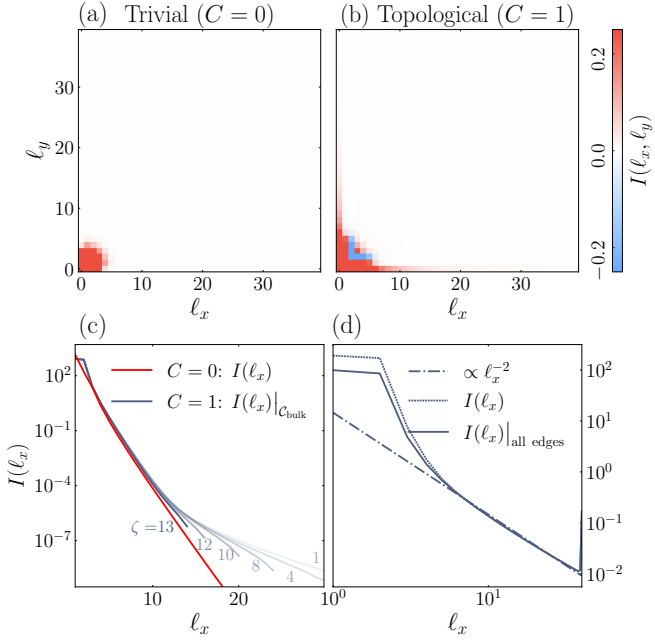


FIG. 9. Information per multiscale $I(\ell_x, \ell_y)$ in the ground state of the $p_x + ip_y$ superconductor on a 40×40 lattice in (a) the trivial phase ($\mu = 6t$, Chern number $C = 0$) and (b) the topological phase ($\mu = 2t$, Chern number $C = 1$). In the trivial ground state the information per multiscale is highly localized at short scales, while in the topological ground state it extends in the direction of 1D chain subsystems ($\ell_x = 0$ or $\ell_y = 0$). (c) The quasi-1D information per scale $I(\ell_x)$ in the trivial ground state (red line) decays exponentially with scale. (d) The quasi-1D information per scale $I(\ell_x)$ in the topological ground state (dotted line) decays algebraically with scale as ℓ_x^{-2} (dash-dotted line). By separating $I(\ell_x)$ into bulk and edge contributions, $I(\ell_x)|_{C_{\text{bulk}}} + I(\ell_x)|_{\text{all edges}}$, we observe that the largest contribution at large scales come from the information on the edges (solid line). The remaining bulk contribution $I(\ell_x)|_{C_{\text{bulk}}}$ in the topological ground state is represented in (c) (gray curves). It approaches the exponential decay of the trivial ground state as the distance ζ (whose value labels each gray curve) between the edges and the bulk subsystem C_{bulk} is increased. $I(\ell_x)|_{C_{\text{bulk}}}$ is normalized so that it sums to $N_x \times N_y$ bits.

tions, we consider further reduced quantities that retain the positional resolution. For the topological ground state, we can isolate the local scaling behavior of the edges from that of the bulk. We split the information per multiscale into two distinct local contributions $I(\ell) = I(\ell)|_{C_{\text{bulk}}} + I(\ell)|_{\text{all edges}}$. The first term in the sum is the bulk contribution at scale ℓ given by $I(\ell)|_{C_{\text{bulk}}}$ following Eq. (12), where C_{bulk} denotes a large rectangular subsystem positioned in the middle of the system, taken to be at a distance ζ away from all edges [orange region in Fig. 10(a)]. The second term is defined as the difference between the total information per multiscale and the bulk one $I(\ell)|_{\text{all edges}} = I(\ell) - I(\ell)|_{C_{\text{bulk}}}$ and hence describes the contributions coming from subsystems near the edges. In Fig. 9(c), we show the corresponding quasi-1D informa-

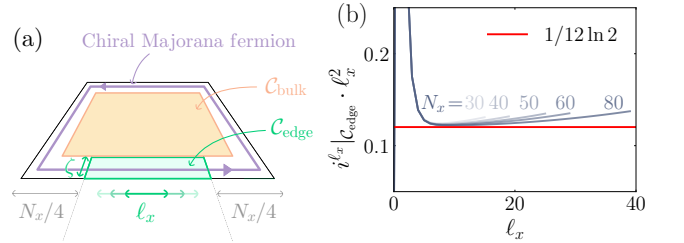


FIG. 10. (a) The topological ground state $|\Psi_{\text{TSC}}\rangle$ of the $p_x + ip_y$ superconductor supports a single chiral Majorana edge state at the boundary (represented in lilac). (b) The average value of the quasi-1D local information [Eq. (23)] along the edge $i^{\ell_x}|_{C_{\text{edge}}}$ at each scale inside the subsystem C_{edge} [shown in green in (a)] that covers the bottom edge. The subsystem C_{edge} spans half the system horizontally ($N_x/2$) and has vertical scale $\zeta = 3$. The scaling follows $i^{\ell_x}|_{C_{\text{edge}}} = \alpha \ell_x^{-2}$ as the system size N_x is increased, with $\alpha = 1/(12 \ln 2)$ the universal scaling constant for a single chiral Majorana fermion.

tion per scale $I(\ell_x)|_{C_{\text{bulk}}}$ [Eq. (14)] for increasing values of ζ . We find that as ζ increases and C_{bulk} is deeper in the bulk, the closer $I(\ell_x)|_{C_{\text{bulk}}}$ approximates the exponentially decaying information distribution of the trivial ground state (red curve). The scaling of the edge information is shown in Fig. 9(d) for $\zeta = 13$, which asymptotically scales as $\propto \ell_x^{-2}$, and where the rapid convergence between $I(\ell_x)$ and $I(\ell_x)|_{\text{all edges}}$ is due to the exponential decay of $I(\ell_x)|_{C_{\text{bulk}}}$ observed in Fig. 9(c). Therefore, by considering the appropriate summation of inclusion-exclusion information inside a region, locally coexisting scaling behaviors in a system can be isolated from each other.

We examine the scaling of information on the edge more closely. The edge theory of a two-dimensional symmetry-protected topological state is one-dimensional scale-invariant [119]. In scale-invariant 1D states, the average local information value at each scale i^{ℓ} takes the form $i^{\ell} = \alpha \ell^{-2}$, where different values of $\alpha = \frac{c_L + c_R}{6 \ln 2}$ correspond to different universality classes, namely $c_{L/R}$ denotes the central charge of the modes of each chirality (left and right moving) [11, 40, 77]. In our case, we have a single Majorana fermion with a chirality fixed by the sign of μ , which we (arbitrarily) refer to as the right-mover; thus, $c_R = 1/2$, $c_L = 0$ and we expect $\alpha = 1/(12 \ln 2)$. To isolate the 1D scaling along the edge, we consider the quasi-1D local information $i_{n_x}^{\ell_x}|_{C_{\text{edge}}}$ in Eq. (13) inside a subsystem C_{edge} positioned along the bottom edge. C_{edge} has position $(0, N_x/4 - 1)$ and multiscale $(N_x/2 - 1, \zeta)$, and is illustrated in green in Fig. 10(a). For generality we consider the average value of $i_{n_x}^{\ell_x}|_{C_{\text{edge}}}$ at each scale

$$i^{\ell_x}|_{C_{\text{edge}}} = \frac{1}{N} \sum_{n_x} i_{n_x}^{\ell_x}|_{C_{\text{edge}}} \quad (23)$$

with $N = N_x/4 - \ell_x$ the number of subsystems at scale ℓ_x . In Fig. 10(b) we find that $i^{\ell_x}|_{C_{\text{edge}}}$ approaches $\alpha \ell_x^{-2}$

with $\alpha = 1/(12 \ln 2)$. The information lattice captures the universal scaling of the chiral channel in the two-dimensional setting. More broadly, its spatially resolved viewpoint may provide a route to diagnosing richer edge features, such as finite-size effects, global boundary conditions, and localized edge defects.

C. Topological order in the toric code

Finally, we consider the toric code, which is defined on a square lattice with a spin- $\frac{1}{2}$ degree of freedom on every edge, as illustrated in Fig. 11(a). Its Hamiltonian is

$$\hat{H}_{\text{TC}} = - \sum_s \hat{A}_s - \sum_p \hat{B}_p, \quad (24)$$

$$\hat{A}_s = \prod_{i \in \text{star}(s)} \hat{X}_i, \quad \hat{B}_p = \prod_{i \in \text{plaquette}(p)} \hat{Z}_i, \quad (25)$$

where \hat{X}_i and \hat{Z}_i denote the x and z Pauli operators on site i , respectively. The star \hat{A}_s and plaquette \hat{B}_p operators are illustrated in Fig. 11(a). Since all star \hat{A}_s and plaquette \hat{B}_p operators commute, the ground-state manifold of the toric code is the simultaneous +1 eigenspace of all \hat{A}_s and \hat{B}_p . We write the corresponding eigenvalues as $A_s = +1$ and $B_p = +1$, referring to them as the star and plaquette *constraints* that define the ground-state sector [120]. Products of Pauli operators along paths define string operators. A string operator $\hat{\gamma}_z = \prod_i \hat{Z}_i$ supported on a path of edges in the direct lattice [green line in Fig. 11(a)] anticommutes with the star operators at its endpoints. Therefore, applying $\hat{\gamma}_z$ to the ground state creates two excitations with $A_s = -1$ at the endpoints of the string. These endpoint excitations are the e anyons, and we refer to such string operators as e strings. Similarly, a string operator $\hat{\gamma}_x = \prod_i \hat{X}_i$ supported on a path of edges on the dual lattice [orange line in Fig. 11(a)] flips the two plaquette eigenvalues at its endpoints to $B_p = -1$. These excitations are the m anyons, and we refer to the string as an m string. A string with no endpoints, that is, a closed e or m string (or *loop*), creates no excitations and leaves the ground state unchanged. Therefore, the ground state is the equal-weight superposition of all possible loop configurations (i.e., the states obtained by acting with all loop operators on a reference state) [121, 122]. This loop picture reflects the topological order of the toric code: contractible loops leave the ground state unchanged, while non-contractible loops distinguish different topological sectors on manifolds with nontrivial topology. The loop structure also manifests in the area law of the von Neumann entropy as $S(\mathcal{A}) = |\partial\mathcal{A}| - \gamma$, where the offset $\gamma = 1$ bit is the topological entanglement entropy [81, 82] and $|\partial\mathcal{A}|$ is the length of the boundary for a subsystem \mathcal{A} assumed to be larger than the correlation length. The topological term γ arises from a single global \mathbb{Z}_2 constraint on the boundary configurations: loops must cross the boundary of \mathcal{A} an even number of times, halving the number

of allowed boundary configurations compared to a trivial gapped state [82].

To characterize the toric code ground state on the information lattice, we first consider the infinite plane without boundaries, where the ground state is unique. An explicit expression for the ground state is

$$|\Psi_{\text{TC,inf}}\rangle = \prod_p \frac{(\hat{1} + \hat{B}_p)}{\sqrt{2}} |+\rangle^{\otimes N} \quad (26)$$

where $|+\rangle$ denotes spin up in the basis of \hat{X} and $N \rightarrow \infty$ is the number of qubits. The product over the plaquette terms generates the superposition of all contractible loop configurations. We examine the reduced density matrix $\rho_{\mathcal{A}}$ of $|\Psi_{\text{TC,inf}}\rangle$ on a subsystem \mathcal{A} which consists of $N_x \times N_y = 6 \times 6$ plaquettes, so that \mathcal{A} has plaquette-type boundaries, as indicated by a dashed contour in Fig. 11(a). We decompose the total information contained in $\rho_{\mathcal{A}}$ across the subsystems \mathcal{C}_n^{ℓ} of \mathcal{A} using the inclusion-exclusion information (6). For the decomposition, we take the subsystems \mathcal{C}_n^{ℓ} as the unions and intersections of plaquettes. For example, the subsystem $\mathcal{C}_{(00)}^{(11)}$ is the single plaquette subsystem at the bottom left corner of \mathcal{A} , shown in lilac in Fig. 11(a). The subsystem $\mathcal{C}_{(12)}^{(03)}$, also indicated in lilac in Fig. 11(a), consists of three vertical edges adjacent to plaquettes (it is the intersection between the two plaquette columns $\mathcal{C}_{(02)}^{(13)}$ and $\mathcal{C}_{(12)}^{(13)}$). Since these subsystems are rectangular, the inclusion-exclusion information takes the form (10). One may also choose a finer or coarser resolution of subsystems (that is, decomposing the information into units smaller or larger than a plaquette). In the present case we use plaquette subsystems, which is suitable for plaquette-type boundaries. If \mathcal{A} instead had star-type boundaries, an equivalent construction would be carried out on the dual lattice using star subsystems.

The information lattice of $\rho_{\mathcal{A}}$ is shown in Fig. 11(b). The single-site subsystems at scales $\ell = (1 0)$ (horizontal edges) and $\ell = (0 1)$ (vertical edges) contain no information about the state: their reduced density matrices are maximally mixed. More generally, all subsystems that are strictly one-dimensional, i.e., those that contain only horizontal or vertical open strings such as $\ell = (\ell 0)$ or (0ℓ) for any $\ell > 1$, also contribute no information. Instead, all the information of $\rho_{\mathcal{A}}$ is located at scales $\ell = (1 1)$ and $\ell = (2 2)$ with genuine two-dimensional extent, which correspond to the subsystems that contain single plaquettes and single stars [123], respectively. Each of these two-dimensional subsystems contributes exactly 1 bit of information, i.e., a single yes/no question, inferred from its density matrix: this corresponds to the definite \mathbb{Z}_2 value of the associated plaquette or star constraint [122, 124]. This reflects the loop picture of the toric code ground state and its \mathbb{Z}_2 topological order. We also see that the state is *local* as there is no information at larger scales: this means that $\rho_{\mathcal{A}}$ does not contain more information about the distribution of measurement outcomes on \mathcal{A} than the reduced density matrix

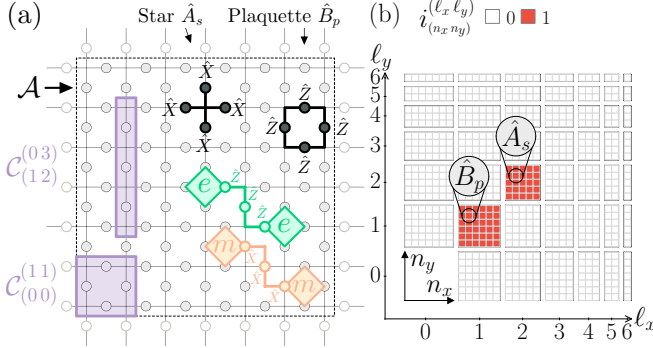


FIG. 11. (a) In the toric code, star \hat{A}_s and plaquette \hat{B}_p operators (represented in black) act on spins (gray dots) located on the edges of a square lattice. The ground state satisfies the constraints $A_s = +1$ and $B_p = +1$ everywhere, while excited states correspond to pairs where these constraints are flipped in sign: a pair of e -anyons (green square) ($A_s = -1$) is created by a string $\hat{\gamma}_z$ (green line) and a pair of m -anyons (orange square) ($B_p = -1$) is created by a string $\hat{\gamma}_x$ (orange line). We consider a subsystem of 6×6 plaquettes \mathcal{A} (dashed line) of the toric code ground state on the infinite plane and its density matrix $\rho_{\mathcal{A}}$. Its subsystems are labeled $\mathcal{C}_{(n_x, n_y)}^{(\ell_x, \ell_y)}$ by groups of plaquettes (and their intersections), with (n_x, n_y) the coordinate of the bottom left corner and (ℓ_x, ℓ_y) their multiscale; two examples $\mathcal{C}_{(0,0)}^{(1,1)}$ and $\mathcal{C}_{(1,2)}^{(0,3)}$ are shown in lilac. (b) The inclusion-exclusion information (10) is evaluated for $\rho_{\mathcal{A}}$ on all subsystems $\mathcal{C}_{(n_x, n_y)}^{(\ell_x, \ell_y)}$. The information of $\rho_{\mathcal{A}}$ is located in all the star and plaquette subsystems, each contributing 1 bit of information. No new information is present at larger scales.

ces on the star and plaquette subsystems. Therefore, the information in the toric code in the planar geometry is exclusively encoded in the local star and plaquette constraints. This is different in nontrivial topologies (e.g., on the torus) where long-range information is contained in non-contractible loops.

The information lattice for excited states is identical to that of the ground state [Fig. 11(b)], regardless of the shape and length of the string that connects the anyons. All subsystems other than those containing a single star or plaquette still contribute 0 bits, which reflects the fact that all possible paths connecting the two anyons are physically indistinguishable. The only information carried by the excited state is the location of the anyons, encoded in the negative eigenvalues of the corresponding star or plaquette operators.

Next, we consider the ground state of the toric code on a finite system with open boundaries, representing an interface between the topologically ordered phase and a trivial gapped phase (the vacuum). We take a system of $N_x \times N_y = 6 \times 6$ plaquettes, as illustrated in Fig. 12(a). With plaquette boundary conditions, the star operators \hat{A}_s are absent on the boundary. We denote edge and corner stars by \hat{A}_s^\perp and \hat{A}_s^\square , respectively, as shown in Fig. 12(a). If the Hamiltonian does not act on these boundary stars, the ground state is highly degenerate because the edge degrees of freedom remain uncon-

strained [125]. We lift this degeneracy by adding small boundary terms, so the Hamiltonian becomes

$$\hat{H}_{\text{TC,open}} = \hat{H}_{\text{TC}} - \frac{\epsilon}{2} \left(\sum_s \hat{A}_s^\perp + \sum_s \hat{A}_s^\square \right) \quad (27)$$

$$\hat{A}_s^\perp = \prod_{i \in \text{edge star}(s)} \hat{X}_i, \quad \hat{A}_s^\square = \prod_{i \in \text{corner star}(s)} \hat{X}_i. \quad (28)$$

Here \hat{H}_{TC} [defined in (24)] acts on all stars and plaquettes in the finite system, and $\epsilon > 0$ is the energy cost of flipping an edge or a corner star. Since \hat{A}_s^\perp and \hat{A}_s^\square commute with all star and plaquette operators, their eigenvalues are $+1$ in the ground state, which defines the set of boundary constraints. The ground state $|\Psi_{\text{TC,open}}\rangle$ is unique and has the same form as Eq. (26), with the product running over all plaquettes in the finite system. Unlike in the infinite system, where only closed strings leave the state in the ground-state sector, the presence of boundaries allows some open strings to do so as well. For a plaquette-type boundary, an m string can be applied from one boundary to another without producing any excitations [for example, the orange line in Fig. 12(a)], while for a star-type boundary the same holds for e strings. In this sense, an anyon can be created or absorbed by the boundary at zero energy cost. This is the phenomenon of anyon condensation (or string condensation) at the boundary [126–128].

The information lattice for $\rho = |\Psi_{\text{TC,open}}\rangle \langle \Psi_{\text{TC,open}}|$ is shown in Fig. 12(b). As in the infinite case of Fig. 11(b), the stars and plaquettes each contribute 1 bit at their respective scales. There are now additional contributions from the four corner stars at scales $\ell = (1, 1)$ and from the edge stars at $\ell = (1, 2)$ and $(2, 1)$, indicated with circular insets in Fig. 12(b). Just like the star and plaquette constraints, each \mathbb{Z}_2 boundary constraint contributes 1 bit. However, the total information contributed by all subsystems with $\|\ell\| \leq 2$ is 61 bits, while the full state contains only $I(\rho) = 60$ bits. This signals an overlap redundancy among the reduced density matrices of $|\Psi_{\text{TC,open}}\rangle$ on the subsystems at these scales. Indeed, one operator is not independent: the product of all star-like operators is the identity,

$$\prod_s \hat{A}_s \prod_s \hat{A}_s^\perp \prod_s \hat{A}_s^\square = \hat{1}, \quad (29)$$

so one of the constraints in the ground state can be inferred from all the others. This redundancy is analogous to the familiar constraint on the torus: the product of all star operators and, separately, the product of all plaquette operators each equals the identity. The overcounted 1 bit at $\|\ell\| \leq 2$ is removed at the largest scale: summing the inclusion-exclusion values over all subsystems whose horizontal or vertical extent spans the full system [the vertices inside the green contour in Fig. 12(b)] yields -1 bit. For an arbitrary topological entanglement entropy,

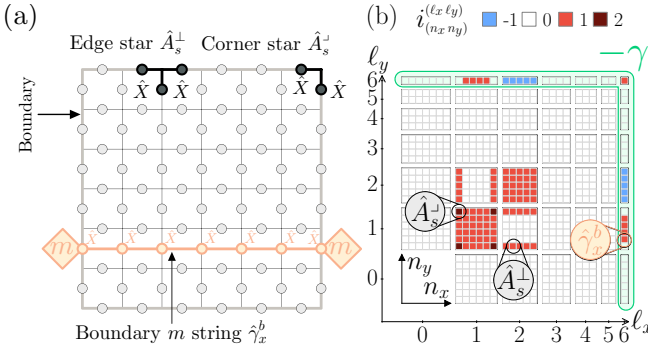


FIG. 12. (a) Toric code on a 6×6 finite system with plaquette-type open boundaries. Because the usual star operators \hat{A}_s are not defined at the boundary, they are replaced by edge stars \hat{A}_s^\perp and corner stars \hat{A}_s° (shown in black). In the ground state of Eq. (27), their eigenvalues are fixed at $+1$, which defines the set of boundary constraints. An m string denoted $\hat{\gamma}_x^b$ connecting two boundary qubits (orange) acts trivially on this ground state. Its endpoints correspond to m anyons absorbed by the boundary, illustrating anyon condensation. (b) The ground state of Eq. (27) is represented on the information lattice. Boundary subsystems (edge and corner stars) each contribute 1 bit of information. At scales $\ell = (1, N_y)$ and $(N_x, 1)$ (plaquette columns or rows stretching from one boundary to the other), the boundary m -string $\hat{\gamma}_x^b$ contributes 1 bit, but this contribution is redundant: at the next scales $\ell = (2, N_y)$ and $(N_x, 2)$ a corresponding negative value appears, as two such strings together form a loop already generated by products of star operators. A global redundancy appears only when the full boundary is included (green contour). The sum of the inclusion-exclusion information values over the full boundary equals -1 bit, which signals the redundancy between the boundary operators in Eq. (29). For an arbitrary topological entanglement entropy, this value is $-\gamma$.

the total large-scale contribution reduces to

$$\sum_{(\ell_x=N_x) \vee (\ell_y=N_y)} \sum_{\mathbf{n}} i_{\mathbf{n}}^{\ell} = -\gamma. \quad (30)$$

Furthermore, the information value at the largest scale is $i_{(00)}^{(N_x N_y)} = \gamma$. This follows algebraically from the inclusion-exclusion information: at the largest scale $\mathbf{n} = (0 0)$, $\ell = (N_x N_y)$, every term in Eq. (10) is the information of a subsystem that touches the open boundary, except the last term $I_{\mathbf{n}+(11)}^{\ell-(22)}$ (a centered subsystem reduced by two unit vectors along each axis). For any subsystem that touches the open boundary, the topological entanglement entropy is zero: any loop that straddles the subsystem boundary can be deformed into a string that condenses at the open boundary, so its topological contribution is lost [129]. Hence, the only term that carries γ at the largest scale is $I_{\mathbf{n}+(11)}^{\ell-(22)}$. Meanwhile, the short-range (area-law) contributions are already fully accounted for at the smaller scales in the information lattice, so they cannot affect the value of $i_{(00)}^{(N_x N_y)}$.

The negative values at scales $\ell = (N_x 2)$ and $(2 N_y)$ can be explained by an analogous reasoning using loops. At scales $\ell = (N_x 1)$ and $\ell = (1 N_y)$ (plaquette rows and columns respectively), the information of the boundary m string $\hat{\gamma}_x^b$ shown in Fig. 12(a) contributes new information. Indeed, within a subsystem of this scale, there are no star operators, and the operator $\hat{\gamma}_x^b$ is independent of all the others inside of that subsystem, so the reduced density matrix provides genuine new predictive power over measurement outcomes on this subsystem. However, at the next scales $\ell = (N_x 2)$ and $(2 N_y)$, negative values indicate that some information was redundant: indeed, a pair of, e.g., horizontal string operators $\hat{\gamma}_x^b$ combined with edge and corner stars forms a loop, which is identical to a product of star operators, hence the correction at this scale. This redundancy is only observed once the subsystem is large enough to contain the full loop.

Altogether, the information lattice recovers the universal topological term γ by exploiting string condensation at the boundaries. This provides an alternative to the von Neumann entropy subtractions of bulk subsystems of Refs. [81, 82, 130]. The same logic applies in the presence of domain walls: if the interior region of size $N_x \times N_y$ has topological entanglement entropy γ_1 and the exterior has γ_2 , then both Eq. (30) and the top-scale value $i_{(00)}^{(N_x N_y)} = \gamma$ remain valid, with γ replaced by $\gamma_1 - \gamma_2$.

We finally discuss the signature of non-Abelian excitations on the information lattice. In the toric code, bringing two anyons of the same type together merges the endpoints of the string that created them, turning the open string into a loop. This means the anyons fuse to the vacuum (the ground state), expressed by the fusion rules $e \otimes e = m \otimes m = 1$. The fusion of an e and m anyon (i.e., the eigenvalues of adjacent star and plaquette are flipped to -1) results in a bound state denoted as $e \otimes m = \varepsilon$, which is fermionic [120]. The toric code anyons are Abelian because their fusion rules assign a single definite outcome to fusing any two anyons. As a result, they leave no signature in the information lattice. To see how this changes in the non-Abelian case, we consider the planar toric code with a line defect whose endpoints are non-Abelian. A line defect [lilac line in Fig. 13(a)] is a lattice dislocation along which the roles of star and plaquette operators are interchanged: dragging an e anyon across the line defect converts it into an m anyon, and vice versa, as shown in Fig. 13(a) [131]. The endpoints of this line defect are so-called twists τ , which behave as Ising anyons and obey the non-Abelian fusion rule $\tau \otimes \tau = 1 \oplus \varepsilon$. The two possible fusion outcomes $\{1, \varepsilon\}$ caused by the presence of a line defect forms a two-dimensional space, and thus a two-fold degeneracy of the ground state, even on the infinite plane. This fusion space can be labeled by the ± 1 eigenvalues of a nonlocal fermionic parity operator \hat{P} , and braiding of the twists is described by a unitary acting on this fusion space [132]. To implement the defect in a Hamiltonian formulation, we modify the toric-code Hamiltonian (24) by replacing

the plaquette operators along the defect with mixed operators, e.g., $\hat{B}_p^{\text{line}} = \hat{Z}_{i_1} \hat{Z}_{i_2} \hat{X}_{i_3} \hat{X}_{i_4}$ where the operator order follows the clockwise ordering of edges starting from the left edge of the plaquette. To preserve commutativity, the star operators straddling the line defect are modified analogously, $\hat{A}_s^{\text{line}} = \hat{X}_{i_1} \hat{X}_{i_2} \hat{Z}_{i_3} \hat{Z}_{i_4}$ assuming the same order. Everywhere else, the Hamiltonian remains identical to that of the toric code [133]. For a single line defect, all pure states in the two-dimensional ground-state manifold give identical subsystem entropies. In particular, for any subsystem \mathcal{C} that encloses exactly one twist, $S(\rho_{\mathcal{C}}) = |\partial\mathcal{C}| - \log d_{\tau}$ with $d_{\tau} = \sqrt{2}$ the quantum dimension of the twist τ , independent of which ground state is chosen [134]. Therefore, we consider any ground state of the infinite planar toric code with a line defect.

We take a region of $N_x \times N_y = 6 \times 6$ plaquettes of the infinite plane with a single line at the position illustrated in Fig. 13(a). In the information lattice shown in Fig. 13(b), we observe that subsystems enclosing a single twist show a reduction of information, which is recovered in the subsystem that encloses both twists. This is similar to the information lattice for singlets in Fig. 4(a): a pair of twist defects τ possesses a two-dimensional fusion space $\{1, \varepsilon\}$, so the ground state can be a superposition of these fusion channels. Note that, unlike a spin- $\frac{1}{2}$ singlet which contributes 1 bit, each twist contributes only $\frac{1}{2}$ bit. This reflects the fact that a pair of twists carries the two-dimensional fusion space of two Majorana zero modes [131, 135]. This nonlocal two-dimensional fusion space is a hallmark of non-Abelian anyons. The information lattice not only identifies the presence of twist defects from their entanglement signatures but also provides a natural framework for tracking non-Abelian braiding operations across position and scale. Specifically, it can be used to determine, at each stage of a braid, which twist pairings have a definite fusion outcome (1 or ε), although we do not analyze this systematically here.

In the toric code on a torus, the presence of non-contractible loops results in a fourfold degeneracy. The information lattice analysis proceeds analogously, showing that part of the state information resides at the largest scales corresponding to these loops. We leave the full analysis of the information lattice for systems with nontrivial topology for future work.

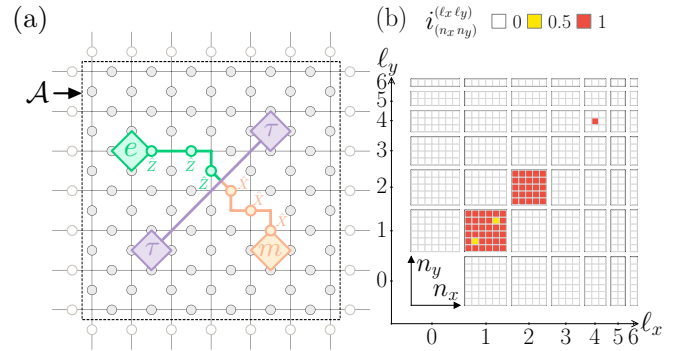


FIG. 13. (a) In the toric code, a line defect (lilac line) is a lattice defect that turns e -anyons into m -anyons (as shown by the green-orange line). The endpoints of the line defect host twist defects τ (lilac squares) with non-Abelian fusion $\tau \otimes \tau = 1 \oplus \varepsilon$, where $\varepsilon = e \otimes m$ is the fermionic excitation that flips both a star and an adjacent plaquette operator. We consider the toric code ground state on the infinite plane, where such a line defect is introduced at the indicated location on a 6×6 plaquette subsystem \mathcal{A} on the plane. (b) The information lattice of $\rho_{\mathcal{A}}$ is similar to Fig. 11(b), except that the subsystem enclosing a single twist contains $\frac{1}{2}$ bit less information. This lost contribution is recovered in the subsystem that encloses both twists. Thus, the information lattice resolves the fusion channels of the non-Abelian defects across position and scale.

V. CONCLUSION

We introduced a higher-dimensional information lattice to characterize many-body quantum states in spatial dimensions greater than one. In periodic chains and in higher-dimensional geometries, overlapping subsystems may form loops. This makes a strictly local assignment of information to each subsystem impossible: the same information may be shared nonlocally across spatially distinct yet overlapping regions, such that it cannot be assigned to any one of them alone. To address this intrinsic issue, we defined the *inclusion-exclusion local information*, which decomposes the total information of subsystem reduced density matrices into position- and scale-resolved contributions. The inclusion-exclusion local information is assigned to the vertices on a higher-dimensional lattice, which are labeled by the position and scales of all subsystems. This construction reveals how information is distributed in a quantum state: a positive value of the inclusion-exclusion local information indicates a net gain of information when considering a larger subsystem of the physical lattice relative to its smaller-scale subsystems. Instead, a negative value signals that part of this information is already inferable from the joint distributions of measurement outcomes of its smaller-scale overlapping subsystems: this signals that overlap redundancies are present in the state. In this way, the higher-dimensional information lattice turns the complexity of higher-dimensional geometries into a structured, position- and scale-resolved description of how in-

formation is organized in quantum many-body states.

We demonstrated through several examples that our decomposition isolates universal features of quantum states in higher dimensions. For the two-dimensional Anderson model, we use quasi-one-dimensional information quantities derived from the inclusion-exclusion information to characterize different states. In the localized ground state of the disordered phase, these quasi-1D information distributions decay exponentially with subsystem scale. This allows us to define information-based intrinsic lengths along different directions, analogous to the intrinsic lengths defined for localized states in one dimension [40]. In the clean critical ground state quasi-1D information distributions instead decay algebraically with scale, and the inclusion-exclusion information defines a preferred direction of information propagation that aligns with the average Fermi velocity orientation, suggesting an information-based approach to Fermi-surface criticality. We then considered a topological state with chiral edge modes, namely, the chiral $p_x + ip_y$ superconductor in its topological phase. In the ground state, the inclusion-exclusion information isolates bulk and edge contributions: the bulk local information decays exponentially with subsystem size away from the open boundary, while the edge contribution exhibits the universal power-law scaling associated with a chiral Majorana edge mode. We then considered the topologically ordered ground state of the toric code. On the infinite plane without boundaries, the information lattice shows that all information is carried locally by star and plaquette constraints. With open boundaries, the inclusion-exclusion information shows features associated with string condensation at the edges, and the topological entanglement entropy appears as a residual contribution at the largest scales of the lattice. Finally, line defects with twist endpoints appear as local contributions on the information lattice. In a non-Abelian braiding protocol, the information lattice points out the location and scale of the channels which produce definite fusion outcomes. This provides an information-based diagnostic of non-Abelian defects and a framework for tracking their braiding across position and scale.

Several directions for future work remain. On the static side, a systematic analysis of critical states using the information lattice could clarify how information propagation directions encode higher-dimensional universality classes, in particular, in the case of higher codimension gapless manifolds [80] and interacting Fermi surfaces [78, 136–139]. Our construction also lends itself to more complex instances of stabilizer surface codes, as the precise location of all stabilizer generators is mapped on the lattice. This opens the possibility to study long-range nonstabilizerness in higher dimensions [62]. A natural direction is to investigate whether our construction can resolve the local structure of domain walls between

distinct topological orders with different anyon contents, even when the topological entanglement entropy is the same. Our local description of information can help identify at what scale and location spurious contributions to the topological entanglement entropy are generated [140–143]. It is natural to apply the information lattice beyond pure ground states, for instance to mixed-state quantum phases, where one would like to characterize when local noise or dynamical processes preserve or destroy topological features [144, 145]. In coding-decoding problems, the study of information currents across scales may provide a scale-resolved understanding of decodability phase transitions and of the conditions under which information remains recoverable [145–147]. Applying our construction to systems on nontrivial topologies, where different winding sectors carry distinct information patterns, we expect the information lattice to be well suited for resolving how information is stored across these topological sectors.

On the dynamical side, a key challenge is to understand how information flows in higher-dimensional lattices and whether hydrodynamic regimes of information, similar to those identified in one dimension [39, 41, 44], can be established in other dimensions as well. Adapting Local Information Time Evolution and related information-recovery methods [39, 44], potentially in combination with sequential reconstruction schemes or cluster expansions [148–151], would open the door to information-lattice algorithms for efficient time evolution and information flow in higher dimensions.

ACKNOWLEDGMENTS

We thank David Aceituno Chávez, Carlo W. J. Beenakker, Maria Hermanns, David J. Luitz, Vieri Mattei and Achim Rosch for useful discussions. This work received funding from the European Research Council (ERC) under the European Union’s Horizon 2020 research and innovation program (Grant Agreement No. 101001902) and the Knut and Alice Wallenberg Foundation (KAW) via the project Dynamic Quantum Matter (2019.0068). T. K. K. acknowledges funding from the Wenner-Gren Foundations. C. A. acknowledges funding by the Deutsche Forschungsgemeinschaft (DFG, German Research Foundation) under Projekt-nummer 277101999 – CRC 183 (project A01). The computations were enabled by resources provided by the National Academic Infrastructure for Supercomputing in Sweden (NAIIS), partially funded by the Swedish Research Council through grant agreement no. 2022-06725.

DATA AVAILABILITY

The data underlying the figures in this work will be made available at Zenodo.

[1] B. Zeng, X. Chen, D.-L. Zhou, X.-G. Wen, *et al.*, *Quantum information meets quantum matter* (Springer, 2019).

[2] N. Laflorencie, Quantum entanglement in condensed matter systems, *Phys. Rep.* **646**, 1 (2016).

[3] J. Eisert, M. Cramer, and M. B. Plenio, Colloquium: Area laws for the entanglement entropy, *Rev. Mod. Phys.* **82**, 277 (2010).

[4] B. M. Terhal, Quantum error correction for quantum memories, *Rev. Mod. Phys.* **87**, 307 (2015).

[5] C. H. Bennett and D. P. DiVincenzo, Quantum information and computation, *Nature* **404**, 247 (2000).

[6] S. Ryu and T. Takayanagi, Holographic derivation of entanglement entropy from the anti-de Sitter space/conformal field theory correspondence, *Phys. Rev. Lett.* **96**, 181602 (2006).

[7] M. Van Raamsdonk, Building up spacetime with quantum entanglement, *Gen. Relativ. Gravit.* **42**, 2323 (2010).

[8] B. Swingle, Entanglement renormalization and holography, *Phys. Rev. D* **86**, 065007 (2012).

[9] M. Srednicki, Entropy and area, *Phys. Rev. Lett.* **71**, 666 (1993).

[10] G. Vidal, J. I. Latorre, E. Rico, and A. Kitaev, Entanglement in quantum critical phenomena, *Phys. Rev. Lett.* **90**, 227902 (2003).

[11] P. Calabrese and J. Cardy, Entanglement entropy and quantum field theory, *J. Stat. Mech.* **2004**, P06002 (2004).

[12] M. M. Wolf, F. Verstraete, M. B. Hastings, and J. I. Cirac, Area laws in quantum systems: Mutual information and correlations, *Phys. Rev. Lett.* **100**, 070502 (2008).

[13] D. N. Page, Average entropy of a subsystem, *Phys. Rev. Lett.* **71**, 1291 (1993).

[14] L. Vidmar and M. Rigol, Entanglement entropy of eigenstates of quantum chaotic hamiltonians, *Phys. Rev. Lett.* **119**, 220603 (2017).

[15] E. Bianchi, L. Hackl, M. Kieburg, M. Rigol, and L. Vidmar, Volume-law entanglement entropy of typical pure quantum states, *PRX Quantum* **3**, 030201 (2022).

[16] S. R. White, Density matrix formulation for quantum renormalization groups, *Phys. Rev. Lett.* **69**, 2863 (1992).

[17] S. Östlund and S. Rommer, Thermodynamic limit of density matrix renormalization, *Phys. Rev. Lett.* **75**, 3537 (1995).

[18] U. Schollwöck, The density-matrix renormalization group in the age of matrix product states, *Ann. Phys. (Amsterdam)* **326**, 96 (2011).

[19] A. C. Doherty, P. A. Parrilo, and F. M. Spedalieri, Detecting multipartite entanglement, *Phys. Rev. A* **71**, 032333 (2005).

[20] S. Szalay, Multipartite entanglement measures, *Phys. Rev. A* **92**, 042329 (2015).

[21] M. Walter, D. Gross, and J. Eisert, Multipartite entanglement (Wiley Online Library, 2016) pp. 293–330.

[22] L. Pezzé and A. Smerzi, Entanglement, nonlinear dynamics, and the Heisenberg limit, *Phys. Rev. Lett.* **102**, 100401 (2009).

[23] P. Hyllus, W. Laskowski, R. Krischek, C. Schwemmer, W. Wieczorek, H. Weinfurter, L. Pezzé, and A. Smerzi, Fisher information and multiparticle entanglement, *Phys. Rev. A* **85**, 022321 (2012).

[24] G. Tóth, Multipartite entanglement and high-precision metrology, *Phys. Rev. A* **85**, 022322 (2012).

[25] H. Strobel, W. Muessel, D. Linnemann, T. Zibold, D. B. Hume, L. Pezzé, A. Smerzi, and M. K. Oberthaler, Fisher information and entanglement of non-Gaussian spin states, *Science* **345**, 424 (2014).

[26] P. Hauke, M. Heyl, L. Tagliacozzo, and P. Zoller, Measuring multipartite entanglement through dynamic susceptibilities, *Nat. Phys.* **12**, 778 (2016).

[27] Y. Chen and G. Vidal, Entanglement contour, *J. Stat. Mech.* **2014**, P10011 (2014).

[28] A. Coser, C. De Nobili, and E. Tonni, A contour for the entanglement entropies in harmonic lattices, *J. Phys. A* **50**, 314001 (2017).

[29] A. Rolph, Local measures of entanglement in black holes and CFTs, *SciPost Phys.* **12**, 079 (2022).

[30] S. Singha Roy, S. N. Santalla, J. Rodríguez-Laguna, and G. Sierra, Entanglement as geometry and flow, *Phys. Rev. B* **101**, 195134 (2020).

[31] S. S. Roy, S. N. Santalla, G. Sierra, and J. Rodríguez-Laguna, Link representation of the entanglement entropies for all bipartitions, *J. Phys. A* **54**, 305301 (2021).

[32] S. N. Santalla, G. Ramírez, S. S. Roy, G. Sierra, and J. Rodríguez-Laguna, Entanglement links and the quasiparticle picture, *Phys. Rev. B* **107**, L121114 (2023).

[33] P. Calabrese and J. Cardy, Evolution of entanglement entropy in one-dimensional systems, *J. Stat. Mech.* **2005**, P04010 (2005).

[34] P. Calabrese, F. H. Essler, and G. Mussardo, Introduction to ‘quantum integrability in out of equilibrium systems’, *J. Stat. Mech.* **2016**, 064001 (2016).

[35] P. Calabrese, Entanglement spreading in non-equilibrium integrable systems, *SciPost Phys. Lect. Notes* , 20 (2020).

[36] A. Nahum, J. Ruhman, S. Vijay, and J. Haah, Quantum entanglement growth under random unitary dynamics, *Phys. Rev. X* **7**, 031016 (2017).

[37] M. Mezei, Membrane theory of entanglement dynamics from holography, *Phys. Rev. D* **98**, 106025 (2018).

[38] H. Liu and S. J. Suh, Entanglement tsunami: Universal scaling in holographic thermalization, *Phys. Rev. Lett.* **112**, 011601 (2014).

[39] T. Klein Kvorning, L. Herviou, and J. H. Bardarson, Time-evolution of local information: thermalization dynamics of local observables, *SciPost Phys.* **13**, 080 (2022).

[40] C. Artiaco, T. Klein Kvorning, D. Aceituno Chávez, L. Herviou, and J. H. Bardarson, Universal characterization of quantum many-body states through local information, *Phys. Rev. Lett.* **134**, 190401 (2025).

[41] N. P. Bauer, B. Trauzettel, T. Klein Kvorning, J. H. Bardarson, and C. Artiaco, Local information flow in quantum quench dynamics, *Phys. Rev. A* **112**, 022221 (2025).

[42] C. Artiaco, J. Barata, and E. Rico, Out-of-equilibrium dynamics in a U(1) lattice gauge theory via local information flows: Scattering and string breaking,

arXiv:2510.16101 (2025).

[43] J. Barata, J. Hormaza, Z.-B. Kang, and W. Qian, Hadronic scattering in (1+1)D SU(2) lattice gauge theory from tensor networks, arXiv:2511.00154 (2025).

[44] C. Artiaco, C. Fleckenstein, D. Aceituno Chávez, T. Klein Kvorning, and J. H. Bardarson, Efficient large-scale many-body quantum dynamics via local-information time evolution, *PRX Quantum* **5**, 020352 (2024).

[45] K. Harkins, C. Fleckenstein, N. D’Souza, P. M. Schindler, D. Marchiori, C. Artiaco, Q. Reynard-Feytis, U. Basumallick, W. Beatrez, A. Pillai, M. Hagn, A. Nayak, S. Breuer, X. Lv, M. McAlister, P. Reshetikhin, E. Druga, M. Bukov, and A. Ajoy, Nanoscale engineering and dynamic stabilization of mesoscopic spin textures, *Sci. Adv.* **11**, eadn9021 (2025).

[46] C. D. White, M. Zaletel, R. S. K. Mong, and G. Refael, Quantum dynamics of thermalizing systems, *Phys. Rev. B* **97**, 035127 (2018).

[47] B. Ye, F. Machado, C. D. White, R. S. K. Mong, and N. Y. Yao, Emergent hydrodynamics in nonequilibrium quantum systems, *Phys. Rev. Lett.* **125**, 030601 (2020).

[48] B. Ye, F. Machado, J. Kemp, R. B. Hutson, and N. Y. Yao, Universal Kardar-Parisi-Zhang dynamics in integrable quantum systems, *Phys. Rev. Lett.* **129**, 230602 (2022).

[49] P. Peng, B. Ye, N. Y. Yao, and P. Cappellaro, Exploiting disorder to probe spin and energy hydrodynamics, *Nat. Phys.* **19**, 1027 (2023).

[50] S. Yi-Thomas, B. Ware, J. D. Sau, and C. D. White, Comparing numerical methods for hydrodynamics in a one-dimensional lattice spin model, *Phys. Rev. B* **110**, 134308 (2024).

[51] M. Yang, S. Anand, and K. K. Nielsen, Beyond fragmented dopant dynamics in quantum spin lattices: Robust localization and non-Gaussian diffusion, *Phys. Rev. B* **112**, 165129 (2025).

[52] T. Rakovszky, C. W. von Keyserlingk, and F. Pollmann, Dissipation-assisted operator evolution method for capturing hydrodynamic transport, *Phys. Rev. B* **105**, 075131 (2022).

[53] C. von Keyserlingk, F. Pollmann, and T. Rakovszky, Operator backflow and the classical simulation of quantum transport, *Phys. Rev. B* **105**, 245101 (2022).

[54] Y. Yoo, C. D. White, and B. Swingle, Open-system spin transport and operator weight dissipation in spin chains, *Phys. Rev. B* **107**, 115118 (2023).

[55] J. Lloyd, T. Rakovszky, F. Pollmann, and C. von Keyserlingk, Ballistic to diffusive crossover in a weakly interacting Fermi gas, *Phys. Rev. B* **109**, 205108 (2024).

[56] E.-J. Kuo, B. Ware, P. Lunts, M. Hafezi, and C. D. White, Energy diffusion in weakly interacting chains with fermionic dissipation assisted operator evolution, *Phys. Rev. B* **110**, 075149 (2024).

[57] J. Surace, M. Piani, and L. Tagliacozzo, Simulating the out-of-equilibrium dynamics of local observables by trading entanglement for mixture, *Phys. Rev. B* **99**, 235115 (2019).

[58] M. Frías-Pérez, L. Tagliacozzo, and M. C. Bañuls, Converting long-range entanglement into mixture: Tensor-network approach to local equilibration, *Phys. Rev. Lett.* **132**, 100402 (2024).

[59] J. Wurtz, A. Polkovnikov, and D. Sels, Cluster truncated Wigner approximation in strongly interacting systems, *Ann. Phys.* **395**, 341 (2018).

[60] L. Pastori, M. Heyl, and J. C. Budich, Disentangling sources of quantum entanglement in quench dynamics, *Phys. Rev. Res.* **1**, 012007 (2019).

[61] M. M. Rams and M. Zwolak, Breaking the entanglement barrier: Tensor network simulation of quantum transport, *Phys. Rev. Lett.* **124**, 137701 (2020).

[62] Y. Bilinskaya, M. F. Martínez, S. Ghosh, T. Klein Kvorning, C. Artiaco, and J. H. Bardarson, Witnessing short- and long-range nonstabilizerness via the information lattice, arXiv:2510.26696 (2025).

[63] Q. Miao and T. Barthel, Convergence and quantum advantage of trotterized MERA for strongly-correlated systems, *Quantum* **9**, 1631 (2025).

[64] S. L. Wong and A. C. Potter, Entanglement renormalization circuits for 2d Gaussian fermion states, arXiv:2506.04200 (2025).

[65] Z. Zhang, 2D entanglement from a single Motzkin spaghetti, arXiv:2506.02103 (2025).

[66] Q. Wen, Entanglement contour and modular flow from subset entanglement entropies, *J. High Energy Phys.* **2020** (5), 1.

[67] F. Rottoli, C. Rylands, and P. Calabrese, Entanglement Hamiltonians and the quasiparticle picture, *Phys. Rev. B* **111**, L140302 (2025).

[68] X.-G. Wen, Topological orders in rigid states, *Int. J. Mod. Phys. B* **4**, 239 (1990).

[69] F. Wilczek, Quantum mechanics of fractional-spin particles, *Phys. Rev. Lett.* **49**, 957 (1982).

[70] D. Arovas, J. R. Schrieffer, and F. Wilczek, Fractional statistics and the quantum Hall effect, *Phys. Rev. Lett.* **53**, 722 (1984).

[71] C. Nayak, S. H. Simon, A. Stern, M. Freedman, and S. Das Sarma, Non-abelian anyons and topological quantum computation, *Rev. Mod. Phys.* **80**, 1083 (2008).

[72] H. Casini and M. Huerta, Universal terms for the entanglement entropy in 2+1 dimensions, *Nucl. Phys. B* **764**, 183 (2007).

[73] M. A. Metlitski, C. A. Fuertes, and S. Sachdev, Entanglement entropy in the $O(N)$ model, *Phys. Rev. B* **80**, 115122 (2009).

[74] E. Fradkin and J. E. Moore, Entanglement entropy of 2D conformal quantum critical points: Hearing the shape of a quantum drum, *Phys. Rev. Lett.* **97**, 050404 (2006).

[75] A. B. Kallin, K. Hyatt, R. R. P. Singh, and R. G. Melko, Entanglement at a two-dimensional quantum critical point: A numerical linked-cluster expansion study, *Phys. Rev. Lett.* **110**, 135702 (2013).

[76] D. Gioev and I. Klich, Entanglement entropy of fermions in any dimension and the Widom conjecture, *Phys. Rev. Lett.* **96**, 100503 (2006).

[77] B. Swingle, Entanglement entropy and the Fermi surface, *Phys. Rev. Lett.* **105**, 050502 (2010).

[78] W. Ding, A. Seidel, and K. Yang, Entanglement entropy of Fermi liquids via multidimensional bosonization, *Phys. Rev. X* **2**, 011012 (2012).

[79] M. M. Wolf, Violation of the entropic area law for fermions, *Phys. Rev. Lett.* **96**, 010404 (2006).

[80] M. Pretko, Nodal-line entanglement entropy: Generalized Widom formula from entanglement Hamiltonians,

Phys. Rev. B **95**, 235111 (2017).

[81] A. Kitaev and J. Preskill, Topological entanglement entropy, Phys. Rev. Lett. **96**, 110404 (2006).

[82] M. Levin and X.-G. Wen, Detecting topological order in a ground state wave function, Phys. Rev. Lett. **96**, 110405 (2006).

[83] F. Verstraete, V. Murg, and J. Cirac, Matrix product states, projected entangled pair states, and variational renormalization group methods for quantum spin systems, Adv. Phys. **57**, 143 (2008).

[84] J. I. Cirac, D. Pérez-García, N. Schuch, and F. Verstraete, Matrix product states and projected entangled pair states: Concepts, symmetries, theorems, Rev. Mod. Phys. **93**, 045003 (2021).

[85] W. McGill, Multivariate information transmission, Trans. IRE Prof. Group Inf. Theory **4**, 93 (1954).

[86] H. K. Ting, On the amount of information, Theory Probab. Appl. **7**, 439 (1962).

[87] S. Watanabe, Information theoretical analysis of multivariate correlation, IBM J. Res. Dev. **4**, 66 (1960).

[88] For example, if there is an observable whose repeated measurements on a single-qubit state ρ always yield the same outcome, then the measurement answers one yes/no question with certainty, resulting in one bit of information (meaning ρ is pure). In contrast, if for every observable the outcomes of repeated measurements are fully random, they provide no information (meaning ρ is maximally mixed). $I(\rho)$ is the average number of independent yes/no questions that can be answered from ρ about the outcomes of measurements.

[89] M. Wilde, *Quantum information theory* (Cambridge university press, 2013).

[90] E. H. Lieb and M. B. Ruskai, Proof of the strong subadditivity of quantum-mechanical entropy, J. Math. Phys. **14**, 1938 (1973).

[91] P. Hayden, R. Jozsa, D. Petz, and A. Winter, Structure of states which satisfy strong subadditivity of quantum entropy with equality, Commun. Math. Phys. **246**, 359 (2004).

[92] Consider a four-site open-boundary 1D chain with sites labeled a, b, c and d . If $|\psi\rangle = |\uparrow\rangle \otimes \frac{|\uparrow\downarrow\rangle - |\downarrow\uparrow\rangle}{\sqrt{2}} \otimes |\uparrow\rangle$ is the state, but we assume the subsystem bc is discarded from the lattice, then the decomposition enforces that $i_{abc} = I(\rho_{abc}) - I(\rho_{ab}) - I(\rho_c)$. This would assign the 2 bits of information associated to the singlet on bc to abc instead. However, it would also assign those bits somewhere else on the lattice, namely to bcd . This structural ambiguity cannot occur if all subsystem intersections each have their own vertex on the lattice.

[93] G.-C. Rota, On the foundations of combinatorial theory: I. Theory of Möbius functions, in *Classic Papers in Combinatorics* (Springer, 1964) pp. 332–360.

[94] R. P. Stanley, *Enumerative Combinatorics, Volume 1*, 2nd ed., Cambridge Studies in Advanced Mathematics (Cambridge University Press, 2011) Ch.2, “Sieve Methods”, Sec.2.1 “Inclusion–Exclusion”.

[95] The information per scale in non-trivial topologies, work in progress.

[96] R. W. Yeung, A new outlook on shannon’s information measures, IEEE Trans. Inf. Theory **37**, 466 (1991).

[97] A. J. Bell, The co-information lattice, in *Proceedings of the 4th International Symposium on Independent Component Analysis and Blind Signal Separation (ICA2003)* (Nara, Japan, 2003) Available online.

[98] P. L. Williams and R. D. Beer, Nonnegative decomposition of multivariate information, arXiv:1004.2515 (2010).

[99] F. E. Rosas, P. A. Mediano, M. Gastpar, and H. J. Jensen, Quantifying high-order interdependencies via multivariate extensions of the mutual information, Phys. Rev. E **100**, 032305 (2019).

[100] R. Horodecki, P. Horodecki, M. Horodecki, and K. Horodecki, Quantum entanglement, Rev. Mod. Phys. **81**, 865 (2009).

[101] If we have the events A : “it is cloudy”, B : “it is raining”, and C : “the ground is wet”, the pairwise distributions $p(A, B)$, $p(B, C)$, and $p(A, C)$ all describe the shared likelihood of rain, clouds and wet ground: knowing the distribution of one gives us some amount of predictive power over the others. Indeed, if we do not know B , then $p(A)$ gives us some predictive power over C , so $I(A : C|\emptyset) > 0$. But if we do know B (i.e., we know it is raining), then $p(A)$ provides less predictive power over C , since once we know it is raining, knowing whether it is cloudy becomes redundant for predicting whether the ground is wet. Thus $I(A : C|B) < I(A : C|\emptyset)$ and, correspondingly, $I(A : B : C) = I(A : C|B) - I(A : C|\emptyset) < 0$, signaling the redundancy. On the other hand, if A, B are uniform Bernoulli distributed random variables and $C = A \oplus B$ is the mod(2) addition, then we have that each marginal density $p(A)$, $p(B)$, and $p(C)$ describes fully random outcomes and therefore carries no predictive power about the others. Similarly $p(A, B), p(B, C), p(C, A)$ also give no predictive power over measurement outcomes. In this case, only by knowing $p(A, B, C)$ we can fully predict what one of the random variables will output, so in this case $I(A : B : C) = 1$ bit > 0 gives new information compared to what the marginal densities provide. See Ref. [152] for a detailed discussion.

[102] If we define the operator $\Delta_x I_n^\ell = I_n^\ell - I_n^{\ell-(1\ 0)} - I_n^{\ell-(1\ 0)} + I_n^{\ell-(2\ 0)}$ (defined analogously for y), then i_n^ℓ can be compactly expressed as $i_n^\ell = \Delta_y \Delta_x I_n^\ell$. If the information does not depend on position (a perfectly homogeneous system where $I_n^\ell = I_{n'}^\ell$ for any $n \neq n'$), the same operator simplifies as $\Delta_x I^\ell = I^\ell - 2I^{\ell-(1\ 0)} + I^{\ell-(2\ 0)}$ which is a second-order (backward) finite-difference of I^ℓ in the ℓ_x component. See e.g. Ref. [93, 94].

[103] P. W. Anderson, Absence of diffusion in certain random lattices, Phys. Rev. **109**, 1492 (1958).

[104] E. Abrahams, *50 years of Anderson Localization*, Vol. 24 (World Scientific, 2010).

[105] I. Peschel, Calculation of reduced density matrices from correlation functions, J. Phys. A **36**, L205 (2003).

[106] E. Abrahams, P. W. Anderson, D. C. Licciardello, and T. V. Ramakrishnan, Scaling theory of localization: Absence of quantum diffusion in two dimensions, Phys. Rev. Lett. **42**, 673 (1979).

[107] F. Evers and A. D. Mirlin, Anderson transitions, Rev. Mod. Phys. **80**, 1355 (2008).

[108] I. T. Jolliffe, *Principal Component Analysis*, 2nd ed., Springer Series in Statistics (Springer, New York, 2002) section 1.1, “Definition and Derivation of Principal Components”, p. 5.

[109] For a subsystem \mathcal{C} we can write the Widom formula as $S(L) = \frac{1}{(2\pi)^{d-1}} \frac{L^{d-1} \log L}{6} \int_{\partial\mathcal{C}} \int_{\partial\Gamma} \Theta(\hat{n} \cdot \hat{v}_F) (\hat{n} \cdot \hat{v}_F) dS_x dS_p$ where $\partial\mathcal{C}$ is the subsystem boundary and \hat{n} its normal, $\partial\Gamma$ is the Fermi surface and \hat{v}_F its normal, and $\Theta(\cdot)$ the Heaviside step function. L is the linear dimension of \mathcal{C} . Assuming \mathcal{C} is a rectangular subsystem, we can then write this compactly as an integral over space, where each boundary normal in space is weighted with an average Fermi vector orientation $\langle \hat{v}_F \rangle$ as $S(L) = \frac{1}{(2\pi)^{d-1}} \frac{L^{d-1} \log L}{6} \int_{\partial\mathcal{C}} |\hat{n}| \cdot \langle \hat{v}_F \rangle dS_x$ where we defined the average Fermi vector orientation as $\langle \hat{v}_F \rangle = \int_{\partial\Gamma} |\hat{v}_F| dS_p$ where in both equations $|\cdot|$ denotes the element-wise absolute value. $\langle \hat{v}_F \rangle$ is the Fermi-surface average of the unit vector representing the local angle of the Fermi velocity with respect to the surface.

[110] N. Read and D. Green, Paired states of fermions in two dimensions with breaking of parity and time-reversal symmetries and the fractional quantum Hall effect, *Phys. Rev. B* **61**, 10267 (2000).

[111] D. A. Ivanov, Non-abelian statistics of half-quantum vortices in p -wave superconductors, *Phys. Rev. Lett.* **86**, 268 (2001).

[112] G. Volovik, Fermion zero modes on vortices in chiral superconductors, *JETP Lett.* **70**, 609 (1999).

[113] A. C. Potter and P. A. Lee, Multichannel generalization of Kitaev's Majorana end states and a practical route to realize them in thin films, *Phys. Rev. Lett.* **105**, 227003 (2010).

[114] The Hamiltonian in Eq. (22) is obtained by discretizing the continuum $p_x + ip_y$ Hamiltonian of Read and Green given by Eq. (1) in [110], where we instead assumed the momentum space pairing $\Delta_{\mathbf{k}} = i\Delta(k_x + ik_y)$ with Δ constant, via the substitution $k_{\mu} \rightarrow \sin k_{\mu}$ and $k_{\mu}^2 \rightarrow 2(1 - \cos k_{\mu})$ in both components $\mu \in \{x, y\}$. With this convention, the topological regime $\mu > 0$ of the continuum corresponds to $|\mu| < 4t$ on the lattice [113, 115, 116].

[115] D. Asahi and N. Nagaosa, Topological indices, defects, and Majorana fermions in chiral superconductors, *Phys. Rev. B* **86**, 100504 (2012).

[116] M. Sato, Topological properties of spin-triplet superconductors and Fermi surface topology in the normal state, *Phys. Rev. B* **79**, 214526 (2009).

[117] S.-Q. Shen, W.-Y. Shan, and H.-Z. Lu, Topological insulator and the dirac equation, in *Spin*, Vol. 1 (World Scientific, 2011) pp. 33–44.

[118] C. Beenakker, Search for non-abelian Majorana braiding statistics in superconductors, *SciPost Phys. Lect. Notes* **15** (2020).

[119] C.-K. Chiu, J. C. Y. Teo, A. P. Schnyder, and S. Ryu, Classification of topological quantum matter with symmetries, *Rev. Mod. Phys.* **88**, 035005 (2016).

[120] A. Y. Kitaev, Fault-tolerant quantum computation by anyons, *Ann. Phys.* **303**, 2 (2003).

[121] M. A. Levin and X.-G. Wen, String-net condensation: A physical mechanism for topological phases, *Phys. Rev. B* **71**, 045110 (2005).

[122] A. Hamma, R. Ionicioiu, and P. Zanardi, Bipartite entanglement and entropic boundary law in lattice spin systems, *Phys. Rev. A* **71**, 022315 (2005).

[123] In our resolution of subsystems, a single star does not correspond to a dedicated star-shaped subsystem; instead it appears at the center of a 2×2 plaquette subsystem, i.e., at scale $\ell = (2, 2)$. This reflects only the coarse graining of our subsystem decomposition: with a resolution of subsystems finer than the plaquette coarse graining, the information associated with individual stars can be assigned uniquely to star-shaped subsystems (not shown here).

[124] D. Fattal, T. S. Cubitt, Y. Yamamoto, S. Bravyi, and I. L. Chuang, Entanglement in the stabilizer formalism, [arXiv:0406168](https://arxiv.org/abs/0406168) (2004).

[125] Y. Cheipesh, L. Cevolani, and S. Kehrein, Exact description of the boundary theory of the kitaev toric code with open boundary conditions, *Phys. Rev. B* **99**, 024422 (2019).

[126] S. B. Bravyi and A. Y. Kitaev, Quantum codes on a lattice with boundary, [arXiv:quant-ph/9811052](https://arxiv.org/abs/quant-ph/9811052) (1998).

[127] S. Beigi, P. W. Shor, and D. Whalen, The quantum double model with boundary: condensations and symmetries, *Commun. Math. Phys.* **306**, 663 (2011).

[128] A. Kitaev and L. Kong, Models for gapped boundaries and domain walls, *Commun. Math. Phys.* **313**, 351 (2012).

[129] For a single plaquette subsystem \mathcal{A} in the bulk, the four stars $\hat{A}_1, \dots, \hat{A}_4$ straddling the boundary satisfy $\hat{A}_1 \hat{A}_2 \hat{A}_3 \hat{A}_4 = \hat{1}_{\mathcal{A}}$ within \mathcal{A} , so the boundary eigenvalues obey $A_1 A_2 A_3 A_4 = +1$ and only 2^3 boundary configurations remain. This redundant parity constraint reduces the von Neumann entropy by 1 bit, described by the offset $\gamma = 1$ bit [82]. If \mathcal{A} touches a trivial (condensing) boundary, the relation instead involves an internal edge or corner star (e.g. $\hat{A}_1 \hat{A}_2 \hat{A}_3 = \hat{A}_b$), so there is no constraint purely among boundary eigenvalues and the topological contribution disappears.

[130] I. H. Kim, Perturbative analysis of topological entanglement entropy from conditional independence, *Phys. Rev. B* **86**, 245116 (2012).

[131] H. Bombín, Topological order with a twist: Ising anyons from an abelian model, *Phys. Rev. Lett.* **105**, 030403 (2010).

[132] H. Zheng, A. Dua, and L. Jiang, Demonstrating non-abelian statistics of Majorana fermions using twist defects, *Phys. Rev. B* **92**, 245139 (2015).

[133] Note that Ref. [131] works in another gauge, which is related to the one used here via a local unitary.

[134] B. J. Brown, S. D. Bartlett, A. C. Doherty, and S. D. Barrett, Topological entanglement entropy with a twist, *Phys. Rev. Lett.* **111**, 220402 (2013).

[135] J. C. Teo, T. L. Hughes, and E. Fradkin, Theory of twist liquids: Gauging an anyonic symmetry, *Annals of Physics* **360**, 349 (2015).

[136] R. Shankar, Renormalization-group approach to interacting fermions, *Rev. Mod. Phys.* **66**, 129 (1994).

[137] J. McMinis and N. M. Tubman, Renyi entropy of the interacting fermi liquid, *Phys. Rev. B* **87**, 081108 (2013).

[138] L. Wang and M. Troyer, Renyi entanglement entropy of interacting fermions calculated using the continuous-time quantum Monte Carlo method, *Phys. Rev. Lett.* **113**, 110401 (2014).

[139] N. Ogawa, T. Takayanagi, and T. Ugajin, Holographic Fermi surfaces and entanglement entropy, *J. High Energy Phys.* **2012** (1), 1.

[140] Y. Zhang, T. Grover, A. Turner, M. Oshikawa, and A. Vishwanath, Quasiparticle statistics and braiding from ground-state entanglement, *Phys. Rev. B* **85**,

235151 (2012).

[141] J. Haah, An invariant of topologically ordered states under local unitary transformations, *Commun. Math. Phys.* **342**, 771 (2016).

[142] K. Kato and P. Naaijkens, An entropic invariant for 2d gapped quantum phases, *J. Phys. A* **53**, 085302 (2020).

[143] I. H. Kim, M. Levin, T.-C. Lin, D. Ranard, and B. Shi, Universal lower bound on topological entanglement entropy, *Phys. Rev. Lett.* **131**, 166601 (2023).

[144] S. Sang, Y. Zou, and T. H. Hsieh, Mixed-state quantum phases: Renormalization and quantum error correction, *Phys. Rev. X* **14**, 031044 (2024).

[145] S. Sang, L. A. Lessa, R. S. Mong, T. Grover, C. Wang, and T. H. Hsieh, Mixed-state phases from local reversibility, [arXiv:2507.02292](https://arxiv.org/abs/2507.02292) (2025).

[146] M. J. Gullans and D. A. Huse, Dynamical purification phase transition induced by quantum measurements, *Phys. Rev. X* **10**, 041020 (2020).

[147] S. Sang and T. H. Hsieh, Stability of mixed-state quantum phases via finite Markov length, *Phys. Rev. Lett.* **134**, 070403 (2025).

[148] D. Petz, Sufficiency of channels over von Neumann algebras, *Q. J. Math.* **39**, 97 (1988).

[149] M. Junge, R. Renner, D. Sutter, M. M. Wilde, and A. Winter, Universal recovery maps and approximate sufficiency of quantum relative entropy, in *Annales Henri Poincaré*, Vol. 19 (Springer, 2018) pp. 2955–2978.

[150] S. Vardhan, A. Y. Wei, and Y. Zou, Petz recovery from subsystems in conformal field theory, *J. High Energy Phys.* **2024** (3), 1.

[151] M. S. Leifer and D. Poulin, Quantum graphical models and belief propagation, *Ann. Phys.* **323**, 1899 (2008).

[152] A. Jakulin and I. Bratko, Quantifying and visualizing attribute interactions, [arXiv:cs/0308002](https://arxiv.org/abs/cs/0308002) (2003).